This is a preprint, the final version is subject to change, of the American Mineralogist (MSA)
Cite as Authors (Year) Title. American Mineralogist, in press.
DOI: https://doi.org/10.2138/am-2020-7140

REVISION 2

THE NATURE OF Zn-PHYLLOSILICATES IN THE NONSULFIDE MINA GRANDE AND CRISTAL ZINC DEPOSITS (BONGARÁ DISTRICT, NORTHERN PERU): THE TEM-HRTEM AND AEM PERSPECTIVE

Giuseppina Balassone[1,*], Valentina Scognamiglio[2], Fernando Nieto[3], Nicola Mondillo[1,4], Maria Boni[1,4], Piergiulio Cappelletti[1], Giuseppe Arfè[5]

[1]Dipartimento di Scienze della Terra, dell'Ambiente e delle Risorse, Università degli Studi di Napoli Federico II, Complesso Universitario Monte S. Angelo, Via Cintia 26, 80126 Napoli, Italy

[2] Via Tosi 4, Pozzuoli, Italy

[3]Departamento de Mineralogía y Petrología and IACT, Universidad de Granada, Granada, Spain

[4]Department of Earth Sciences, Natural History Museum, London, UK

[5]Via Staffetta 127, Giugliano, Italy

[*]Corresponding author: balasson@unina.it

RUNNING TITLE: Zn-phyllosilicates in the nonsulfide deposits of Bongará (Peru)

This is a preprint, the final version is subject to change, of the American Mineralogist (MSA)
Cite as Authors (Year) Title. American Mineralogist, in press.
DOI: https://doi.org/10.2138/am-2020-7140

ABSTRACT

Zn-phyllosilicates are common minerals in nonsulfide Zn deposits and can give crucial information on the genesis of these oxidized mineralizations. They seldom represent the prevailing economic species but might have a significant impact on mineral processing. This study has been carried out on the Mina Grande and Cristal Zn-sulfide/nonsulfide deposits, which occur in the Bongará district (Amazonas region, northern Peru). The Cristal and Mina Grande orebodies are hosted by the sedimentary (prevailingly carbonate) successions of the Pucará Group (Condorsinga formation, Lower Jurassic), in an area affected by Neogene tectonics and characterized by Late Miocene and Pliocene-Early Pleistocene uplift phases (Andean and Quechua tectonic pulses). The Cristal deposit consists of both sulfide (sphalerite with minor pyrite and galena) and nonsulfide concentrations. The nonsulfides consists of smithsonite, hemimorphite, hydrozincite, chalcophanite, goethite and greenockite, locally associated with Zn-bearing phyllosilicates. The Mina Grande deposit consists almost exclusively of Zn-oxidized minerals in limestone host rocks. The nonsulfides association consists of hydrozincite, hemimorphite, smithsonite, fraipontite and Fe-(hydr)oxides, also containing a clayey fraction. The study deals with TEM-HRTEM and AEM investigations on clayey materials, in order to determine their crystal-chemical features and the origin of the complex Zn-clays-bearing parageneses. In both deposits, Zn-bearing illites ($1M_d$ and $2M$ polytypes) and I/S clay minerals (I3) are the main detected phases, with few compositions close to (Zn-bearing) muscovite. In the clayey fraction at Mina Grande, fraipontite, a Zn-bearing mica called K-deficient hendricksite, and (Zn-bearing) kaolinite also occur. Zn-illites and smectites (always containing Zn in variable amounts) characterize the mineral association at Cristal. The investigated compositional gap between di- and tri-octahedral Zn-phyllosilicates gives indications on the genetic relationships between them and advances on the knowledge of these species. The present work gives an insight into the Zn-bearing phyllosilicates systems, by determining the amount/mode of metal

incorporation in their lattices and understanding the relationships of natural occurring clay-rich complex associations, which can act as models for possible synthetic counterparts.

Keywords: Zn-phyllosilicates; Bongará; Cristal; Mina Grande; Peru; TEM-HRTEM; AEM

INTRODUCTION

Zn-phyllosilicates are quite rare minerals, which can be found in most nonsulfide Zn deposits. In this kind of ores, mainly derived from the weathering of primary sulfide concentrations, the Zn-clays generally represent minor concentrations in the mineral assemblage, but they can also be the prevailing economic minerals as in the world-famous Skorpion deposit in Namibia (Borg et al. 2003; Emselle et al. 2005; Kärner 2006; Boni and Mondillo 2015; Buatier et al. 2016; Choulet et al. 2016; Arfè et al. 2017; Balassone et al. 2017). Zn-clay minerals, formed in slightly acidic to neutral conditions, are also commonly found in contaminated soils at mining and smelting sites (Manceau et al. 2000; Juillot et al. 2003).

Sauconite (Ross 1946; Newman and Brown 1987), one of the most common clay minerals in nonsulfide deposits (Large 2001; Hitzman et al. 2003; Boni, 2005, 2009a,b; Mondillo et al. 2014; Boni and Mondillo 2015), is a trioctahedral saponite-like smectite with Zn in octahedral coordination. Experimental studies on its synthesis and stability (i.e., Kloprogge et al. 1999; Higashi et al. 2002; Petit et al. 2008; Pascua et al. 2010) demonstrated that sauconite can precipitate from solutions of silicic acid, variously mixed with Zn-compounds (Zn-chlorides, Zn-oxides, or Zn-hydroxides) and Na- and Al compounds, at a pH interval of 6–12 and temperatures ranging between 20 and 200 °C. Among the other Zn-phyllosilicates, the mineral fraipontite, belonging to the kaolinite-serpentine group and the serpentine subgroup (Fransolet and Bourguignon 1975), and baileychlore, a member of the chlorite group (Rule and Radke 1988), also occur in some nonsulfide

ore deposits. Recently, Mondillo et al. (2015) and Balassone et al. (2017) studied the Zn-phyllosilicates from Accha and Yanque (Peru) and Skorpion (Namibia), respectively, by means of transmission electron microscopy - high resolution TEM (TEM-HRTEM) analyses. Kaufhold et al. (2015) characterized the Zn-bearing smectites from the Silver Coin Mine (USA). Buatier et al. (2016) and Choulet et al. (2016) described Zn-clays consisting of interstratified fraipontite/smectite (fraipontite-prevailing), closely associated to willemite ores in several nonsulfide Zn deposits from the Moroccan High Atlas, formed by direct precipitation of meteoric and/or hydrothermal fluids.

Generally speaking, Zn-clays are not only an ore resource but also a drawback, because they can negatively affect the industrial treatment to a various extent (Choulet et al. 2016, and references therein). Hence, their detailed mineralogical study is particularly useful from the perspective of industrial and economic evaluations.

Zn-phyllosilicates had been already detected in the Mina Grande and Cristal sulfide and nonsulfide deposits, located in the Bongará area in northern Peru (Arfè et al. 2017a,b, 2018; Arfè 2018; Mondillo et al. 2018a,b). In these mineralizations, sulfide minerals are mostly represented by sphalerite and by minor galena and pyrite, weathered to a nonsulfide assemblage mostly consisting of smithsonite, hemimorphite, and hydrozincite. Arfè et al. (2017b, 2018) and Arfè (2018) detected variable amounts of different Zn- phyllosilicates in the complex mineral assemblages of the Bongará mining district. A first detailed mineralogical identification of the Zn-rich clayely assemblages of the Mina Grande and Cristal supergene deposits was carried out by Arfè et al. (2017a) by combined scanning electron microscopy with energy dispersive X-ray spectroscopy (SEM-EDS) and X-ray powder diffraction (XRPD). According to the latter work, the main sheet silicates occurring in both deposits were considered I/S (illite/smectite) mixed layers, partly altered or overprinted by sauconite. Fraipontite (the Zn-member of the kaolinite-serpentine group) has been found only at Mina Grande, locally associated with minor zaccagnaite (a rare hydrated Zn-Al carbonate, member of the hydrotalcite supergroup and quintinite group; Merlino et al. 2001; Lozano

et al. 2012; Mills et al. 2012), whereas a Zn(Mn) mica similar to hendricksite (a Zn-Mn trioctahedral potassic mica; Robert et al. 1985) was detected at Cristal.

However, due to the micro- to nano-sized nature of the Bongará phyllosilicates, as well as to the presence of diffuse impurities, typically consisting of Fe(Mn)-(hydr)oxides (i.e. goethite, chalcophanite, etc.), some questions still remained open, thus requiring a specific study of the clay fraction. The issues in need of a better clarification concerned: (i) a more accurate characterization of the widespread Zn-layered silicate varieties generically identified as Zn- micas (or illites), as well as of the I/S interstratified clay minerals, (ii) the ascertainment of hendricksite-type mica, (iii) the definition of the smectite(s) types and of other possible clays (or also other possible Zn- minerals), (iv) if the occurrence of fraipontite should be confined only to Mina Grande deposit.

In order to answer these questions and determine the true nature of the Zn- phyllosilicates, we have carried out detailed TEM and scanning TEM (STEM) and HRTEM investigations down to the nanoscale on the clay-rich fraction of a few selected samples already studied by Arfè et al. (2017a). This approach has allowed to analyze the purest mineralogical phases and has consequently helped resolving the issues above exposed. The present research was also aimed at identifying the processes accounting for the genesis of the Zn-phyllosilicates, with implications to their potential for zinc recovery.

GEOLOGY AND MINERALIZATION OF THE BONGARÁ AREA

Bongará is a province of the Amazonas Region in Peru, located approximately 740 km north of Lima and 245 km northeast of the coastal city of Chiclayo. It is situated on the western margin of the Subandean foreland basin of northern Peru, within the mountainous terrain of the Subandean fold-and-thrust belt (Fig. 1a) (Arfè et al. 2018). The geology of the northern Andes, where Bongará is located, underwent two important orogenic cycles (Benavides-Caceres 1999), i.e. the pre-Andean

(Precambrian to Paleozoic) and Andean (Early Jurassic to Present) cycles. The sedimentary Pucará Basin developed in correspondence of the current Estern Cordillera, within a NW-trending sinistral shear zone (Mégard 1987; Benavides-Caceres 1999; Rosas et al. 2007). The basin started to be filled with up to 3000 m thick continental siliciclastics of the Mitu Group (Middle to Late Triassic) (Arfè et al. 2017a, 2018), which include red sandstones, mudstone, polymictic conglomerates and rare pyroclastic rocks (Fig. 1b). At the same time, it underwent a fault-controlled subsidence, which was gradually followed by a regional subsidence associated with NW to NNW-trending sinistral shear zone from Late Triassic to Early Jurassic (Mégard 1984; Benavides-Caceres 1999; Rosas et al. 2007). From Late Triassic to Early Jurassic, the sediments of the Pucará Group filled the basin with shallow- to deep-water marine carbonates, unconformably deposited over the sediments of the Mitu Group (Fontboté 1990; Reid 2001; Rosas et al. 2007). The Pucará Group Units are stratigraphically subdivided in basal Chambará Formation consisting of thinly bedded limestone and silty shale, overlying bituminous calcareous Aramachay Formation and uppermost Condorsinga Formation with its bioclastic and cherty limestone (Brophy et al., 2012). During Toarcian, a regional uplift promoted erosion and karstification of the top of the Condorsinga carbonates (Mondillo et al. 2018a), leading to the formation of cavities and depressions. As a consequence, the continental sequences of the Sarayaquillo Formation (Upper Jurassic to Cretaceous), which consist of red shales, sandstones and marls (Arfè et al. 2017b; Arfè 2018), were deposited in various colluvial, alluvial and lacustrine environments together with gypsum beds (Rosas et al. 2007) in angular unconformity above the Condorsinga Formation (Fontboté 1990; INGEMMET 1995). The lower Cretaceous in the Bongará area is characterized first by a major marine transgression, which led to the deposition of siliciclastic rocks of the Goyllarisquizga Group, and then of argillaceous limestones with nodular silty mudstones (Mondillo et al. 2018a) of the Chonta-Chulec Formation. The area of interest for this study has been affected by Neogene tectonics from 20.5 to 1.6 Ma,

149 characterized by Late Miocene and Pliocene-Early Pleistocene uplift phases, among which the
150 Andean and Quechua tectonic pulses (Arfè et al. 2017a,b, 2018; Arfè 2018; Mondillo et al. 2018a).
151 The Pucará Basin includes many types of ores in central and northern Peru (Kobe 1977, 1982,
152 1990a,b; Dalheimer 1990; Fontboté 1990; Reid 2001), mainly corresponding to Mississippi Valley-
153 type (MVT) Zn-Pb deposits. The most intensive exploration in the Bongará area was carried out in
154 the Charlotte Bongará permit (which includes the Mina Grande and Cristal occurrences) in the
155 north, and in the Florida Canyon permit, in the south. These deposits consist of stratabound Zn-Pb
156 nonsulfide/sulfide concentrations (Wright 2010; Boni and Mondillo 2015). The formation of
157 supergene nonsulfide mineralization is closely related to the tectonics of the area, which led to
158 uplift, uncapping, weathering and alteration of several exhumed sulfide orebodies (Arfè et al.
159 2017b).
160 Mina Grande and Cristal are hosted by Mesozoic limestones and dolostones of the Condorsinga
161 Formation. The Mina Grande deposit consists totally of nonsulfides, derived from the weathering of
162 MVT ores. The mineralization contains supergene zinc minerals such as smithsonite, hemimorphite,
163 hydrozincite but also of Zn-phyllosilicates. Mina Grande was partly mined in open-pit in three
164 different areas (A, B and C Phases) and is currently under exploration. The Cristal deposit is a
165 mixed sulfide and nonsulfide mineralization, with the latter resulting from alteration and dissolution
166 of the sulfide protore. The presence of sulfides still in place at Cristal (Mondillo et al. 2018a)
167 combined with the absence of any obvious recent karstic activity, suggests that supergene alteration
168 acted in two different ways in the two respective localities (Arfè et al. 2018).
169
170
171 **MATERIALS AND METHODS**
172 The transmission electron and analytical electron microscopy (TEM-AEM) study was conducted on
173 four samples (ZB-1, ZB-2, CR07-13, CR13-7) collected from the Mina Grande and Cristal

nonsulfide deposits (Fig. 2), during a field survey carried out in 2016. These (sub)samples come from drill cores and hand-specimens already mentioned in Arfè et al. (2017a). In order to select the richest clayey fractions of the samples for successive TEM-AEM investigations, preliminary mineralogical analyses were carried by combined X-ray powder diffraction (XRPD) and SEM-EDS at the Dipartimento di Scienze della Terra, dell'Ambiente e delle Risorse (DiSTAR) University of Naples Federico II, Italy (XRD equipment: Seifert–GE ID3003 diffractometer, with CuK_{α} radiation, Ni-filtered at 40 kV and 30 mA, 3–80 °2θ range, step scan 0.02°, time 10 s/step, and RayfleX (GE) software package; SEM-EDS equipment: JEOL JSM5310 electron microscope with Oxford EDS, INCA X-stream pulse processor with 4.08 Inca software, operating conditions at of 15 kV and 20 mm working distance).

Textural observation of clays at the micro- and nanoscale and chemical analyses were performed on thin sections by combining TEM with high resolution transmission electron microscopy (HRTEM), scanning transmission electron microscopy (STEM) and high-angle annular dark field (HAADF) investigations, carried out at the Centro de Instrumentación Cientifica (CIC) of the University of Granada (Spain). Copper rings were attached to representative selected areas of the matrix of thin sections prepared with Canada balsam and after ion-thinned, using a Fischione Model 1050 ion mill, and carbon coated. Ion milling was performed at 4 kV and ±10°, until the first hole and ±7° during 20 min for final cleaning. We used a Titan TEM with XFEG emission gun, spherical aberration image corrector and HAADF detector, working at 300 kV, with a resolution of 0.8 Å in the TEM mode and 2 Å in the STEM mode. Qualitative vs. quantitative chemical identification of minerals and chemical maps were obtained by AEM-EDX (energy dispersive X-ray spectroscopy) analyses using the Super-X system. Quantitative analyses, presented in Tables 2-5, were obtained using albite, biotite, muscovite, spessartine, olivine, titanite, and hemimorphite as standards, measured using the same protocol as samples (Abad and Nieto 2003), to obtain K-factors for the transformation of intensity ratios to concentration ratios, according to Cliff and Lorimer (1975). In

order to avoid contamination problems (mainly due to widespread goethite and other oxy-hydroxides), several chemical analyses were rejected, and only those as pure as possible have been accepted. Electron diffraction patterns (selected area electron diffraction, SAED) were carried out, whenever possible, in the same areas investigated by TEM-AEM. Additional investigations on particle morphology and quantitative chemical analyses were obtained by using a TEM Philips CM20 (CIC, Granada), operating at 200 kV, with an EDAX solid-state EDX detector. Lifetime of the analyses was 100 s; areas producing dead time higher than 5% were rejected to ensure the thin character required by the Cliff and Lorimer (1975) approximation. Analyses were obtained using STEM mode, from powdered portions deposited on a holey C-coated Au grid. This mode of preparation disperses individual grains of minerals onto the grid surface. Albite, biotite, muscovite, spessartine, olivine, titanite, and hemimorphite standards were measured using the same protocol as the samples.

Ideal chemical formulae of the main minerals quoted in this work are listed in Table 1.

RESULTS

The TEM-AEM study has pointed out that the main phyllosilicate detected in the clay-rich fractions of the supergene assemblage of Bongará is being identified as illite, which always contains Zn (±Fe,Mn) in variable amounts (Tables 2-5), hence corresponding to a Zn-bearing illite. These chemical variations describe a particular outline and represent, in our opinion, a key point for the definition of this kind of Zn-sheet silicates, as it will be discussed more in detail in the following paragraphs. Taking into account that AEM allows determining the ratios between the various elements, it is required to normalize the obtained chemical compositions to the basic formula of the investigated minerals. Hence, on the basis of the composition of Zn-bearing illites, we have mainly distinguished two varieties:

- Zn(Fe)-poor and Al^{VI}-rich varieties, in brief indicated hereafter as Zn-illites, and considered as dioctahedral. Their structural formulas have been calculated on the basis of 6 (IV+VI) cations, as suggested by Nieto et al. (2010) for dioctahedral species of illite;
- Zn(Fe)-rich and Al^{VI}-poor varieties, which we have considered as a mixture of dioctahedral/trioctahedral species and abbreviated to MDT Zn-illites hereafter (see also Discussion). For these mixed compositions, the structural formulas have been recalculated on the basis of 11 oxygens.

Other significant Zn-bearing mineral/associations have been detected in minor to trace amounts in the two sampled occurrences (Mina Grande and Cristal), and are described in the following paragraphs.

Mina Grande

Tables 2 and 3 show representative AEM analyses of Zn-illite and MDT Zn-illite in the Mina Grande samples (ZB-1 and ZB-2), with the second variety definitely prevailing over the first one.

Zn-illite shows the tetrahedral cations in the range 3.06-3.14 apfu for Si (average, av. hereafter, equal to 3.10 apfu) and 0.86-0.94 apfu for Al^{IV} (av. 0.90 apfu); regarding the octahedral cations, Zn is in the interval 0.31-0.40 apfu (av. 0.36 apfu), Mg 0.19-0.26 apfu (av. 0.23 apfu), Fe 0-0.01 apfu (av. 0.01), Ti 0-0.03 apfu (av. 0.02 apfu), whereas Al^{VI} is in the range 1.31-1.49 apfu (av. 1.40 apfu). The interlayer cation K varies in the range 0.70-0.75 apfu (av. 0.73 apfu). Fig. 3a shows a common texture of Zn-illite, often associated with fraipontite mainly occurring as cavity fillings. The SAED-HRTEM investigations (Fig. 3b) demonstrate that illite is characterized by lattice fringes and 00l spots in the SAED with *d*-spacings always around 10 Å. The rest of the rows (non-00l) in the SAED, which could allow the identification of the mica polytypes, are represented by continuous lines, indicating a disordered polytype $1M_d$. The lattice fringe images of Fig. 3c show misorientation among the packets, typical of illite. The various packets have different

crystallographic orientation, at less [100] and [110] zone axis have been identified from partial periodicity which can be recognized along some layers and allows identification of very local order, corresponding to 1*M* polytype of illite. In the FFT of the image 3c (inset), together with those orientations, also [010] can be identified. The misorientation among the various packets is responsible of the disordered character of the polytype identified for the whole area in the SAED. However, in the same image the textures can be interpreted as belonging to illite/smectite mixed layers (I/S) of I3 type, due to the minor presence of smectite layers, characterized by different contrast and spacing (12 Å), separated by at less 3 illite layers[1]. Smectite layers collapse variably between 17 and 10 Å, being the latter their most frequent value, in the vacuum of the microscope, principally depending on their local interlayer composition (Nieto et al, 1996). Periodicity of 52 Å (4 illite layers + 1 smectite layer) can be also identified in the FFT. Fig. 3e shows a chemical map of a Zn-illite (+fraipontite, Fe,Ti-oxy-hydroxides) area and its typical EDX spectrum, with the small but always present peak of Zn.

Compositions referred as to MDT Zn-illite (Tables 2 and 3) show the tetrahedral cations in the range 2.57-3.17 apfu for Si (av. 2.90 apfu) and 0.83-1.43 apfu for Al^{IV} (av. 1.10 apfu); in the octahedral site, Zn is in the interval 0.29-1.44 apfu (av. 0.77 apfu), Mg 0.15-0.46 apfu (av. 0.26 apfu), Fe up to 0.81 apfu (av. 0.37 apfu), Ti up to 0.52 apfu (av. 0.20 apfu) and Al^{VI} is in the range 0.43-1.42 apfu (av. 0.92 apfu), whereas K is in the interval 0.48-0.90 apfu (av. 0.62 apfu). Fig. 4a shows a textural image of an area of sample ZB-1 particularly rich in MDT Zn-illite; its electron diffraction pattern is shown in the bottom-right inset of Fig. 4a, and represents rows with spacings of 10 Å. Figs. 4b,c,d,e also shows the association of MDT Zn-illite with fraipontite and Fe,Ti,Mn-

[1] The notation I3 refers to the nomenclature for interstratifications as reported by Vázquez et al. (2016) and Bauluz et al. (2000). Indeed, according to these authors, ordering in interstratified I/S, ordinarily characterized by its *Reichweite* value (*R*) based on X-ray diffraction data, representing long-range ordering averaged over all the layers that scatter X-radiation; TEM images can identify short-range ordering of interlayers within I/S packets, and the Reichweite nomenclature results inappropriate for specific layer sequences as observed by TEM. Hence the notation I*n*, analogous to the *Reichweite* nomenclature, can be employed but applied only to specific layers, where *n* is the number of illite-like layers associated with a given smectite-like (see Vázquez et al. 2016, and references therein, for further details).

oxy-hydroxides. The 1:1 phyllosilicate is often in individual recognizable crystals significantly bigger than those of micas, reaching a maximum length of 3 μm.

Fig. 5 shows a remarkable feature involving these Zn-layered silicates and observed in an area of approximately 1 μm^2. Figs. 5a and 5b, respectively, illustrate a textural image and the related chemical map of sample ZB-2, where illites show variable amounts of Zn in the packets; here they occur with fraipontite and subordinate kaolinite and Fe-Ti-oxides. If the AEM map of Fig. 5b is compared with the chemical mappings of selected elements of Fig. 5c, the illite-rich area is significantly well-defined by the K map and displays a complex textural organization. Indeed, in this zone, while K is homogeneously distributed, Zn is highly heterogeneous, resulting in fine intergrowths between MDT Zn-illite, with 1.28 apfu of Zn (see analysis. # 3.cuan-MAP1 of Table 3, and EDX spectrum 2 of Fig. 5d), and Zn-illite, with 0.31 apfu of zinc (see analysis # 6.cuan, Table 3, and EDX spectrum 1 of Fig. 5d). The inference of this particular compositional and textural organization, relevant to the origin of Zn-phyllosilicates, will be discussed more in detail in the section "Discussion". High resolution TEM investigation of this zinc illite (inset in Fig. 5) illustrates stacking of 10 Å periodicity, which is in agreement with this type of sheet silicate.

Another second distinctive finding in the Mina Grande samples is a well-defined Zn-mica (illustrated in Tables 2, 3 and Fig. 6), having an octahedral population with Zn in the range 1.55-1.89 apfu (av. 1.66 apfu), Fe 0.13-0.20 apfu (av. 0.15 apfu) and Mg up to 0.14 apfu (av. 0.15 apfu), (Tables 2 and 3); Si is the range 2.87-2.92 apfu (av. 2.89 apfu) and Al^{IV} 1.08-1.13 apfu (av. 1.11 apfu), whereas K shows an interval of 0.57-0.70 apfu (av. 0.64 apfu) (Tables 2 and 3). In accordance with the guidelines reported in the classification of micas (Rieder et al. 1998), hendricksite is characterized by Zn>1.5 apfu and K<1. Hence the Zn-mica detected here can be defined as hendricksite, even if this mica typically shows an “illitic” character (lower K amounts, presence of Al^{VI}). For this reason, we named it K-deficient hendricksite. Fig. 6 shows Zn-phyllosilicates dispersed particles in sample ZB-2, composed of K-deficient hendricksite, Zn-illite

and fraipontite, with the qualitative chemical spectra of selected areas of the zinc mica and serpentine.

Fraipontite was detected in the Mina Grande samples. Fig. 3d shows stacking of 7 Å periodicity, typical of this Zn phyllosilicate. Fig. 4c illustrates an association of fraipontite and MDT Zn-illite at the nanoscale; the electron diffraction pattern in the inset suggests an epitaxial or topotaxial relationship between the two minerals, as they share the *c** parameter. Due to the paragenetic relations between these 2:1 and 1:1 phyllosilicates, it is reasonable to assume that fraipontite grew onto illite. Chemical compositions of fraipontite (Tables 2 and 3) show tetrahedral cations within a range of 1.08-1.40 apfu for Si (av. 1.23 apfu) and 0.60-0.92 apfu for Al^{IV} (av. 0.76 apfu); the octahedral cations range from 2.19 to 2.96 apfu for Zn (av. 2.54 apfu), from 0.34-0.68 apfu for Al^{VI} (av. 0.50 apfu) and from 0.04 to 0.14 apfu for Fe (av. 0.10 apfu).

Kaolinite was detected in very subordinate amounts only in sample ZB-2 (Table 3). In the tetrahedral site Si is in the range of 2.00-2.10 apfu (av. 2.05 apfu), whereas the octahedral population is composed of 1.44-1.66 apfu Al^{VI} (av. 1.54 apfu), as well as of small amounts of Mg (0.13 apfu) and Zn (0.12-0.70 apfu, av. 0.14 apfu).

Finally, Fig. 7a and 7b respectively show HAADF and chemical mapping of an area of sample ZB-2 where tiny cavity-lining and tapering crystals of supposed zaccagnaite can be observed together with Zn-illite, fraipontite and oxides (Table 1). These crystals are Zn-rich and appear morphologically slightly different from fraipontite crystals; the EDX spectrum displays high Zn, C and O peaks, compatible with a zinc carbonate, whereas the chemical map of Si indicates the virtual absence of this element in the areas of possible zaccagnaite occurrence. Even though smithsonite/hydrozincite could also be a reasonable option, the occurrence of zaccagnaite in the Mina Grande samples has been already proved by Arfè et al. (2017a). Because of the nano-sized dimension of these crystals and the close association with fraipontite, it was impossible to obtain chemical analyses and SAED-HRTEM images for validating this phase.

320

321 **Cristal**

322 Similarly to Mina Grande, also in the Cristal samples CR07-13 and CR13-7 (Fig. 2) illites, both Zn-
323 and MDT Zn-illites, are always the prevailing minerals detected in the supergene assemblage. Here
324 the varieties referred as Zn-illite prevail over the MDT types (Tables 4 and 5), if compared with
325 Mina Grande. Furthermore, differently from Mina Grande, and in agreement with Arfè (2018), K-
326 deficient hendricksite and fraipontite have been not detected, at least in the investigated samples.
327 In the Cristal Zn-illites (Tables 4 and 5), the tetrahedral cations are in the range 3.18-3.66 apfu for
328 Si (av. 3.36 apfu) and 0.42-0.82 apfu for Al^{IV} (av. 0.64 apfu); in the octahedral site, Zn is in the
329 interval of 0.04-0.27 apfu (av. 0.10 apfu), Mg 0.16-0.32 apfu (av. 0.29 apfu), Fe up to 0.21 apfu (av.
330 0.11), whereas Al^{VI} is in the range 1.41-1.11 apfu (av. 1.50 apfu). Regarding the interlayer cation K,
331 it varies in a range of 0.34-0.72 apfu (av. 0.61 apfu). As illustrated in Tables and 5, few values of K
332 indicate compositions close to a (Zn-bearing) muscovite, rather than illite. In particular, if we
333 consider three analyses of sample CR07-13 (Table 4, # anl. 5, anl. 11 and 1.cuan-MAP2) and two
334 analyses of sample CR13-7 (Table 5, # 3.cuan-MAP4 and 11.cuan-MAP5) in relation to the ideal
335 muscovite formula established by Rieder at al. (1998), these compositions fulfill the condition of
336 the interlayer cation (K) amounts in the range 0.7-1.0 apfu (or $I \geq 0.85$ apfu), as well as the
337 condition of Si = 3.0-3.1 apfu in the majority of cases; however, the ^{VI}Al values of these analyses
338 do not fully satisfy the standard muscovite ranges reported by Rieder at al. (1998) (1.9-2.0 apfu),
339 and also most of the calculated $^{VI}R^{2+}/(^{VI}R^{2+} + {}^{VI}R^{3+})$ ratios are slightly higher (0.30 apfu on average)
340 than the muscovite range (i.e. <0.25 apfu). These Zn-bearing muscovites show the following
341 ranges: Si 2.89-3.39 apfu (av. 3.19 apfu) and Al^{IV} 0.61-1.811 apfu (av. 0.81 apfu), with Al^{VI} 0.90-
342 1.66 (av. 1.50 apfu), Zn 0.07-0.15 apfu (av. 0.11 apfu), Mg 0-0.29 apfu (av. 0.18 apfu), Fe up to
343 0.84 apfu (av. 0.29) and Mn 0-0.65 apfu (av. 0.12 apfu) in the octahedral site. The interlayer cation
344 K is in the range 0.81-1.07 apfu (av. 0.95 apfu).

Fig. 8 shows the chemical mapping of Zn-illite, which can contain differently Zn-enriched packets varying from Zn of 0.04 apfu (see analysis # 3.cuan-MAP1 of Table 4 and EDX spectrum 1 of Fig. 8c) to Zn equal to 0.21 apfu (see analysis # 1.cuan-MAP1 of Table 4 and EDX spectrum 2 of Fig. 8c). The SAED-HRTEM investigation is reported in Fig. 8b, where rows with stacking of 10 Å periodicity can be observed.

Subordinate MDT Zn-illite (Tables 4 and 5) shows the tetrahedral cations in the range 2.67-2.93 apfu for Si (av. 2.78 apfu) and 1.07-1.33 apfu for Al^{IV} (av. 1.22 apfu); the octahedral cations vary from 0.51-0.60 apfu for Al^{VI} (av. 0.54 apfu), 0.39-0.86 apfu for Zn (av. 0.65 apfu), 0.28-0.98 apfu for Mn (av. 0.72 apfu), 0.60-1.07 apfu for Fe (av. 0.86 apfu) and up to 0.26 apfu for Mg (av. 0.09 apfu). Compared with the same varieties detected at Mina Grande, these illites are Mn-bearing and Ti-free. Due to the rarity of MDT type, it was not possible to find suitable crystalline particles for recording their lattice fringes images and/or electron diffraction patterns of acceptable quality.

Fig. 9a and 9b show typical textural images of the Zn-illite at Cristal. The top right inset of Fig. 9a shows the electron diffraction pattern with differences of orientation among the various packets; rows with periodicity of 14 Å can be due to smectite. In the right inset of Fig. 9b, the less visible row corresponds to [100] (20 Å, 2*M* polytype*)*, and the more visible to [010]. Diffraction points corresponding to (h0l) have systematic extinctions for *l* odd, therefore they do not allow the polytype identification. The left inset of Fig. 9b also illustrates the SAED pattern of a disordered polytype ($1M_d$). Fig. 9c and 9d respectively illustrate lattice image of packets with I/S mixed layers having minor proportion of smectite layers (I3) and slightly disoriented packets, typical of illite.

Fig. 10 illustrates another characteristic of the zinc phyllosilicates at Cristal; here smectite occur both as nanoscale interleaved (Fig. 10a) phase with Zn-illite and in larger particles (Fig. 10b); high resolution TEM images show that the small packets are internally ordered with stacking of 10 Å (Zn-illite) and 13 Å (slightly collapsed smectite) periodicities. Smectites detected in the Cristal samples correspond to beidellite, which always contain small amounts of Zn (0.02 apfu) and

sauconite (see the EDX spectra of Fig. 10 and Table 5). As shown in Fig. 10b, sauconite seems also to replace zinc illite. Finally, a composition attributable to montmorillonite, with small but detectable Zn amount (0.14 apfu) was also locally found (Fig. 10a and Table 5).

Overall crystal-chemical features of the Bongará phyllosilicates

Bivariate diagrams of selected elements of the detected phyllosilicates are reported in Fig. 11. In the Al_{tot} vs. Si diagram (Fig. 11a), zinc illites are generally enriched in these elements compared with MDT Zn-illites, even though some Si-depleted compositions fall in the field of the latter illites. K-deficient hendricksite entirely plots in the area of MDT Zn-illite, being indistinguishable from these illites in terms of Si and Al_{tot} contents. Fraipontites cluster in a well-constrained field, as well as kaolinites. Sauconite compositions are characterized by variable Si and Al amounts, as already observed by Mondillo et al. (2015) and to a lesser extent by Balassone et al. (2017), and possibly attributable, at least in part, to interstratifications with illite layers.

The Zn vs. Al^{VI} plot (Fig. 11b) shows a positive correlation of EDX data, illustrating a distinction between dioctahedral and trioctahedral species; MDT Zn-illite compositions fall in a quite wide area, placed between the Zn-illite and the K-deficient hendricksite fields. MDT Zn-illite is variable in term of both Zn and Al^{VI}, whereas Zn-illites show an evident chemical variability mainly in term of Al^{VI} content. Hendricksite is better constrained if compared with the diagram of Fig. 11a (even though only three compositions were measured at Mina Grande). Obviously, fraipontite/sauconite and kaolinite/beidellite/montmorillonite occupy the opposite sides of trioctahedral and dioctahedral compositional fields, respectively.

Fig. 11c illustrates the Zn vs. K diagram, which shows a similar trend as the previous plot; the dioctahedral and trioctahedral compositions fall in well-defined fields, with MDT Zn-illite compositions scattered between the Zn-illite and the K-deficient hendricksite fields. The major chemical variability of Zn-illite is related to the K cation, differently from MDT Zn-illite

compositions, which are more variable in terms of both Zn and K contents. Indeed, while in bivariate plots of Fig. 11a and 11b compositions approaching muscovite cannot be distinguished from the other Zn-illites, in the diagram of Fig. 11c mica-related compositions are obviously better constrained, due to their higher K amounts. Dioctahedral smectites plot in the Zn, K-poor side.

In the M^{+}-4Si-3R^{2+} ternary diagram (Fig. 12a), used for discriminating the dioctahedral and the trioctahedral compositions (Meunier 2005), our Zn-illites are scattered along the mixing line of muscovite-sauconite-fraipontite ideal compositions and rather plot into an intermediate domain between the muscovite and sauconite poles. As illustrated in Tables 4 and 5, some compositions more correctly plot close to muscovite end-member, whereas other Zn-illites, as well as MDT Zn-illites are more scattered, indicating that clays are generally mixed compositions. In this plot, K-deficient hendricksite also plots along the muscovite-sauconite join and into the MDT Zn-illite field, in slightly different position if compared with the ideal hendricksite. Fraipontite plots very close to the theoretical compound, whereas other clay minerals, i.e. smectites and kaolinite, are more scattered due to their chemical variability (i.e. Zn in kaolinite).

In the K-Zn-Al^{VI} ternary diagram of Fig. 12b all Zn-illites plot into an intermediate area between ideal muscovite and K-deficient hendricksite; Zn-illite, MDT Zn-illites and K-deficient hendricksite occupy three different domains, fairly well-defined but continuous, indicating that zinc clays are dominantly a mixture of two end-members *sensu lato* approaching theoretical muscovite and hendricksite, that we have considered to be respectively Zn-illite and K-deficient hendricksite (see the next paragraph). As might be expected, compositions close to (Zn)muscovite plot in a better defined, K-rich, area. Fraipontite again plots in a restricted field, confirming its homogenous composition, as well as smectites (both dioctahedral and trioctahedral), even if based on few point-analyses.

DISCUSSION

420 **Mineral identification**

421 Guggenheim et al. (2006) listed illite as a dioctahedral species in the interlayer-deficient mica
422 group. However, following the proposal by Rieder et al. (1998), Guggenheim et al. (2007)
423 subsequently considered illite to be only a series name. Besides showing a variety of chemical
424 compositions, many illite samples are essentially mixed-layer structures, with smectite usually
425 making up the other component although the presence of interstratified smectite layers is difficult to
426 detect when their proportion is less than 10%. The chemical composition of illite has been
427 extensively studied by many authors (i.e. Środon and Eberl 1984; Brigatti and Guggenheim 2002;
428 Meunier and Velde 2004; Meunier 2005; Nieto et al. 2010; Escamilla-Roa et al., 2016), and
429 according to the International Mineralogical Association (IMA) nomenclature committee the term
430 illite should be used to designate interlayer-cation-deficient (<0.85 apfu) micas (Rieder et al. 1998).
431 Then, following the nomenclature suggested by Rieder et al. (1998), illite has a general formula
432 $K_{0.65}Al_{2.0}\square Al_{0.65}\ Si_{3.35}\ O_{10}(OH)_2$, with $^{VI}R^{2+}/(^{VI}R^{2+} + {}^{VI}R^{3+}) \leq 0.25$, and can refer to a relatively
433 large volume in compositional space, as a counterpart to glauconite. To summarize, we established
434 that the Zn-illite investigated in the present study, and often reported by Arfè et al. (2017a,b) simply
435 as Zn-mica, is very similar to illite *sensu* Reider et al. (1998); its mean formula can be expressed as:
436
437 $K_{0.67}(Al_{1.45}\ Ti_{0.01}Mg_{0.26}Fe_{0.06}Zn_{0.22})_2(Si_{3.3}Al_{0.7})_4O_{10}(OH)_2 \bullet nH_2O$
438
439 The occurrence of Mg and Fe is a common characteristic for illite, but, if we compare the
440 theoretical formula of illite with this case of study, the remarkable aspect is that its packets also
441 show variable Zn concentration (e.g. Fig. 8). In the ordered illite polytype (mainly observed at
442 Cristal), the apparent disorder is only due to the small dimension of the packets with different
443 orientation and does not reside in the packet itself, as normally observed in illite. At Mina Grande,
444 instead, a true disordered polytype ($1M_d$) has been found. Besides, the minor occurrence of smectite

445 layers, attributable to R3 type I/S mixed layers, has also been observed in the investigated samples
446 (Figs. 3 and 9). Compositions ascribed to Zn-bearing muscovite, found in the Cristal samples only,
447 can be expressed by the average formula $K_{0.95}(Al_{1.30}Mg_{0.18}Fe_{0.29}Mn_{0.12}Zn_{0.11})_2$
448 $(Si_{3.19}Al_{0.81})_4O_{10}(OH)_2 \bullet nH_2O$.
449 Many mixed compositions between Zn-illite and K-deficient hendricksite, i.e. MDT Zn-illites, are
450 recognized in this study. K-deficient hendricksite has the following average empirical formula:
451
452 $K_{0.64}(Al_{0.86}Mg_{0.15}Fe_{0.15}Zn_{1.66})_{2.82}(Si_{2.89}Al_{1.11})_4O_{10}(OH)_2$.
453
454 From the TEM study, this mica appears to be Mn-free, differently from Arfè et al. (2017a,b) and
455 Mondillo et al. (2018a), who found Mn in some Zn-micas from Cristal. Considering that when
456 studying these assemblages at a finer scale (TEM-HRTEM), the mica particles, as well as other zinc
457 silicates, appeared to be often pervaded by Fe(Mn)-(hydr)oxides (Fig. 13), it is possible that
458 previous EDS-WDS analyses could have been carried out on micas with very fine intergrowths of
459 Fe- and Mn-(hydr)oxides. The simple fact that we found a hendricksitic mica at Mina Grande only
460 and not at Cristal, contrary to Arfè et al. (2017a,b) and Mondillo et al. (2018a), can be also due
461 either a heterogeneous nature of the samples or to an intrinsic limit of the sample selection for TEM
462 analyses, which investigated a restricted area in each specimen.
463 In this study, fraipontite was detected at Mina Grande only, in agreement with Arfè et al. (2017a,b),
464 and has the following empirical formula obtained by AEM study:
465
466 $(Zn_{2.54}Fe_{0.10}Al_{0.50})_{3.14}(Si_{1.24}Al_{0.76})_2O_5(OH)_4$.
467
468 Fraipontite commonly occurs in pore spaces and as well-crystallized individuals with dimension in
469 the range 0.2-3 μm, free of inclusions of other minerals (e.g. Figs. 3 and 4). This rare Zn-clay also

crystallized onto the illite surface; indeed, sometimes these two minerals are also in epitaxial/topotaxial relation, with illite acting as a template for the zinc serpentine (Fig. 4c). Contrary to the fraipontite-bearing nonsulfide zinc deposit of Bou Arhous in Morocco (Choulet et al., 2016), at Mina Grande interstratified fraipontite/sauconite minerals were not detected in the fraipontite-rich fractions.

Rare trioctahedral and dioctahedral smectites were also found in the Cristal clay fractions. Sauconite has been found in this location in agreement with the findings of Arfè et al. (2018), who described this smectite as mica replacement, as well as occurring in vugs and fracture fillings; its average composition is:

$K_{0.28}(Zn_{2.34}Mg_{0.12}Al_{0.16}Fe_{0.07}Mn_{0.33})_{3.02}(Si_{3.38}Al_{0.62})_4O_{10}(OH)_2 \bullet nH_2O$.

The average composition of the Accha and Yanque sauconite (Mondillo et al. 2015) is $(Ca_{0.15}K_{0.05})_{0.20}(Zn_{2.10}Mg_{0.20}Al_{0.40}Fe_{0.15}Mn_{0.02})_{2.87}(Si_{3.5}Al_{0.5})_4O_{10}(OH)_2 \bullet nH_2O$. Compared with the latter occurrences, K is the only interlayer cation in the Cristal sauconite, and is also richer in Zn and Mn and poorer in Al^{VI} and Mg.

Together with sauconite, already reported by Arfè et al. (2017a,b, 2018) and Arfè (2018), the first recorded occurrence of beidellite can be observed in the same location, always with a small Zn amount (0.02 apfu). This clay has the following average formula:

$K_{0.19}(Al_{1.81}Mg_{0.24}Zn_{0.02})_{2.07}(Si_{3.70}Al_{0.30})_4O_{10}(OH)_2 \bullet nH_2O$.

If compared with the composition of the Zn-bearing beidellites found in the Accha and Yanque nonsulfide zinc ore deposits (Mondillo et al. 2015), i.e. $(Ca_{0.05}K_{0.15})_{0.20}(Al_{1.6}Zn_{0.25}Mg_{0.1}Fe_{0.15})_{2.1}(Si_{3.6}Al_{0.4})_4O_{10}(OH)_2 \bullet nH_2O$, the Cristal beidellite shows

interlayer cation only represented by K, lower Zn, higher Mg contents and lacking of Fe. Moreover, also a Zn-bearing montmorillonite (0.14 apfu of Zn) occurs at Cristal, perfectly in line with what was observed in all the Bongará layered silicates.

Finally, the kaolinite of Mina Grande has an average formula $(Al_{1.54}Zn_{0.41}Mg_{0.13})_{2.08}Si_{2.05}O_5(OH)$ and shows K in trace amount (0.13 apfu), which indicates minor contamination by surrounding illite in the investigated site and explains the anomalous octahedral and tetrahedral sums found.

The compositional gap between di- and trioctahedral Zn-phyllosilicates

The first major division in the classification of phyllosilicates is between their dioctahedral and trioctahedral varieties. This is due to the different structural configurations of their respective octahedral layers, with concomitant effects on the corresponding linked tetrahedral layers. In the trioctahedral ones, divalent cations (typically Mg and Fe^{2+}) occupy the three possible positions, accounting for a total charge of 2x3 = 6. On the other hand, in the dioctahedral ones, trivalent cations (generally Al, but also frequently Fe^{3+}) occupy only two positions, giving 3x2 = 6 charges. Due to their greater charge, trivalent cations strongly attract anions, producing a smaller octahedron than the divalent ones in the trioctahedral structures, and, certainly smaller than the vacant positions in dioctahedral ones. Therefore, the general structure of the two kinds of layers is significantly different, with three roughly similar octahedrons in the trioctahedral layers, in opposition to two smaller ones and one big irregular position (usually named the *M*1 site) in the dioctahedral structures (Moore and Reynolds 1997).

As a result, the phyllosilicates always correspond to one of the two types of structures, with a consequential compositional gap between both of them, with a very limited possibility of a solid solution. Therefore, phyllosilicates which have an intermediate composition are rare in nature. The cases of midway chemistry are solved by the existence of nanodomains, as the case of smectites, which appear continuous at the clay particle scale, but are made of associated different lattices or

clusters at a finer scale, producing a wide miscibility gap (Grauby et al. 1993; Yamada et al. 1999), or in alternation of the two types of layers, as in sudoite or the limited occurrence of di-trioctahedral interstratified minerals. Therefore, due to the structural constrains, at the unit cell level, a phyllosilicate is either dioctahedral or trioctahedral.

In this context, the compositional maps in Fig. 5b and 5c can be considered a graphic representation of the compositional gap between dioctahedral and trioctahedral 2:1 phyllosilicates for the case of Zn varieties. In the phyllosilicates, due to their crystal-chemical characteristics, atomic radio and charge, Zn plays a similar role to Mg and Fe^{2+}. Therefore, as a major element it tends to form trioctahedral phyllosilicates, similarly to Mg in phlogopite, saponite, serpentines or tri-chlorites. These would be the equivalent cases of hendricksite, sauconite, fraipontite or baileychlore. However, Mg and Fe (together with other divalent cations, e.g. Mn) can also enter in minor proportion in the typical Al dioctahedral phyllosilicates as muscovite-illite, montmorillonite-beidellite or kaolinite. In a similar way, Zn has been detected in this study in all the aforementioned cases (note that the only exception is baileychlore, which does not occur at Bongará). Zn-bearing varieties of illite (muscovite), beidellite, kaolinite and montmorillonite, have been found together with their trioctahedral counterparts, i.e. K-deficient hendricksite, fraipontite and sauconite, in which Zn is the major or the quite unique octahedral cation.

A special consideration needs the case of illite/micas, which are the major constituents of the studied samples. The Cristal and Mina Grande samples mainly consist of Zn-illites. Since they have been formed in a low-temperature environment, these mica-like compositions are genetically conditioned to form as their low-temperature variety, hence to crystallize as illite (Merriman and Peacor 1999; Vázquez et al 2016). Nevertheless, the composition of the fluid from which the micas were grown should have had a Zn content greater than the amount acceptable by the crystal chemistry of dioctahedral illite/mica. Due to the compositional gap between zinc dioctahedral and trioctahedral phyllosilicates, the resultant product was an extremely fine intergrowth of the two

varieties: a Zn-illite and its trioctahedral equivalent, i.e. K-deficient hendricksite with Zn as the major octahedral cation. As pointed out by the AEM study, most of the obtained analyses have been unable to resolve the intergrowth, due to its nano-sized nature, under the 20 nm scale (Fig. 5a), resulting in many mixed compositions, i.e. the so-called MDT Zn-illite, as shown in the bivariate plots of Fig. 11 and in the ternary diagrams of Fig. 12. However, the high spatial capabilities of the modern TEMs have allowed obtaining in some limited areas detailed chemical information (as shown in Fig. 5b and 5c), able to reveal the dual nature of the intergrowths (Fig. 5d).

The trioctahedral Zn-rich limb of the gap for the low-temperature micas (illite) is difficult to classify due to the lack of previously described equivalents. It shares with hendricksite the major component and the trioctahedral nature. Usually, hendricksite contains also a high quantity of Mn (Robert and Gaspérin 1985; Sharygin 2015), but according to the IMA classification of micas (Rieder et al.1998), this characteristic is not a limiting condition for its classification. Our analyses fulfill the condition of Zn>1.5 apfu, hence the mineral with the studied composition could be considered as hendricksite, but this is not considered one of the K-deficient micas in the IMA classification. Indeed, according to Rieder et al. (1998), the trioctahedral phyllosilicate corresponding to an interlayer-deficient mica is named wonesite, which has a formula $Na_{0.5}\square_{0.5}Mg_{2.5}Al_{0.5}AlSi_3O_{10}(OH)_2$; in the IMA database, the chemical formula of this mineral is reported as $(Na,K,\square)(Mg,Fe,Al)_6(Si,Al)_8O_{20}(OH,F)_4$. The term wonesite is used in the sense of trioctahedral equivalent of illite in the clay literature although, admittedly, following Rieder et al. (1998), it appears as a Na, instead of K, variety. In conclusion, we have indicated the trioctahedral Zn-equivalent of illite as a K-deficient hendricksite. Alternatively, a valid name could be Zn(K)-wonesite, even though a proper term was not predicted in the IMA classification as, to our knowledge, this phase had not been previously described in literature.

Origin of the Bongará Zn-phyllosilicates assemblage

570 Illite is a widespread mica-related clay mineral, uncommon as a surface-derived weathering
571 product, generally formed diagenetically from other clay minerals, such as smectite and kaolinite at
572 temperatures higher than of 70 °C (Einsele 2000). According to Meunier (2005), the range of
573 physical conditions for illite formation are from 20 °C, in surface soil conditions, to below 300 °C,
574 under diagenetic or hydrothermal environments. During diagenesis, with increasing burial, the
575 degree of crystallinity of illite increases, leading to more stable structures. Most studies on
576 illitization report that, as I/S interstratified clays become illitic, the interlayer arrangements change
577 from random (R0) to short-range (R1) ordered, and then to long-range (R3) ordered (e.g. Nieto et
578 al. 1996; Vázquez et al. 2014, and references therein). This occurs at temperatures from 75 to 120
579 °C. The transition from R1- to R3-ordered I/S occurs up to 175 °C, or in other cases at also higher T
580 (Vázquez et al. 2014, and references therein).
581 In the context of nonsulfide Zn(Pb) ores, the zinc-rich clays are frequently detected in supergene
582 deposits, although few studies have provided a clear identification of their nature. In addition, the
583 origin of zinc clays and their place within the ore evolution remain poorly understood (Choulet et
584 al. 2016).
585 The AEM study and the TEM-HRTEM textural evidences of the studied samples suggest that Zn-
586 bearing illite, together with the I3 I/S detected both at Cristal and Mina Grande, could be deposited
587 from a Zn-bearing fluid in a temperature range of 170-200 °C. Considering that Mondillo et al.
588 (2018a), using the mineral geothermometer GGIMFis and the trace element data in sphalerite from
589 the Cristal prospect calculated a possible precipitation temperature (TGGIMFis) of 225±50 °C
590 (slightly higher than in the genesis of typical MVT deposits; Paradis et al., 2007), the studied Zn-
591 illite could have formed during (and/or just after) sulfide precipitation; these TOT sheet silicates
592 hosted Zn^{2+} cations in the octahedral site to various degrees, up to hendricksite-like mineral.
593 Regarding Mina Grande, Arfè et al. (2017b) hypothesized that both a Zn-bearing mica and
594 fraipontite could have formed during the hydrothermal alteration of siltstone or sandstone

595 interbedded within the host limestone, in association with the emplacement of sulfides. The
596 evidences obtained in this study seem to support this genetic model.
597 Regarding fraipontite, its textural arrangement observed by means of TEM-HRTEM suggests that
598 this mineral occurs as a newly formed phase from direct precipitation from Zn(Si,Al)-rich fluids
599 (possibly low temperature hydrothermal), likely at expense of Zn-bearing illite. According to recent
600 studies (i.e. Arfè et al. 2017a; Buatier et al. 2016; Choulet et al. 2016), this TO clay mineral may
601 have formed either during the hydrothermal process that generated the Zn sulfides, or in the early
602 stages of supergene alteration, which took place under acidic conditions associated with the
603 alteration of sulfides. In both cases, when the buffering of the carbonate host rock turned the
604 environment from acidic to alkaline (pH>7), the fraipontite became unstable and zaccagnaite started
605 to form at its expenses. Arfè et al. (2017a) described by XRD analysis the occurrence of the 3*R*-
606 polytype zaccagnaite at Mina Grande; they inferred that this particular fraipontite-zaccagnite
607 association could suggest an origin related to weathering processes. However, the present study was
608 not able to definitively confirm or reject this inference about the nature of zaccagnaite and of its
609 origin from a crystal-chemical point of view, because of the tiny size and paucity of their crystals in
610 the samples analyzed.
611

612 **IMPLICATIONS**

613 This study reveals that the whole of virtually Zn-free phyllosilicates in the Bongará district (Peru)
614 do contain zinc in variable amounts. Among these minerals, Zn-illites are the most widespread in
615 the investigated Zn-rich clayey materials. Considering that deciphering the nature of clay minerals
616 is pivotal for direct implications in the mining industry dealing with base metal recovery/processing
617 of Zn and other metals in nonsulfide deposits (Arfè et al. 2017, and references therein), Zn-bearing
618 illites might not be considered as barren material indeed. In addition, this study indicates that zinc is
619 located within the octahedral sites in each component of the layered silicate forming an intricate

mineral assemblage (as also observed in other studies, e.g. Choulet et al. 2016; Balassone et al. 2017). Hence it cannot be recovered easily and can only be released by leaching techniques such as solvent extraction, which is relatively efficient for a given clay species like sauconite (Cole and Sole 2002; Boni 2005; Boni et al. 2009a,b; Boni and Mondillo 2015). At Bongará, as in other worldwide occurrences (Choulet et al. 2016), the subordinate occurrence of interstratified clay minerals can have effects in ore liberation, requiring advances for an efficient separation technique and a better selectivity of solvents used.

Clay minerals are efficient sinks for base and heavy metals in the geosphere (Churakov and Dähn 2012), and the knowledge of the uptake mechanism of these elements on clays, among which there are illite and smectite, can have many important applications in a number of fields of material sciences, including, for instance, protection from industrial pollution and waste, clay based-polymer nanocomposites, heterogeneous catalysts etc. (e.g. Srivastava et al. 2005; Gu and Evans 2007, 2008; Montoya et al. 2018; Zhang et al. 2017). Hence the present work can contribute to an insight into Zn-bearing phyllosilicate systems, by determining the amount/mode of metal incorporation in their lattices and understanding the relationships of naturally occurring complex clay-rich associations, which can act as models for synthetic counterparts.

Finally, this research provides an advance in understanding the compositional gap between dioctahedral and trioctahedral layer silicates, with regard to Zn-poor and Zn-rich clays/micas of Bongará, which corresponds to their di- and tri-octahedral varieties respectively. In this case of study, Zn plays in phyllosilicates an equivalent role to Mg and Fe^{2+}, with minor presence in the dioctahedral species, together with trioctahedral minerals in which Zn is the major octahedral cation. Among others, this is the case of K-deficient hendricksite - or, if any, Zn(K)-wonesite - the low-temperature variety of Zn trioctahedral mica, whose composition has been firstly described in the current study. It can be predicted that other similar examples will be discovered when appropriate (metal-bearing) systems are examined more closely down to the nanoscale.

ACKNOWLEDGEMENTS

The authors are indebted to M.M. Abad-Ortega and C. de la Prada Sánchez (CIC, Granada) for the skilful support during TEM analyses, and to R. de Gennaro (DiSTAR, Napoli) for his invaluable help during SEM analyses. The authors thank two anonymous Referees, who provided constructive reviews that greatly improved the manuscript, and the Associate Editor Andrew E. Madden for handling manuscript. This work was partly supported by Departmental funds 2017 (University of Napoli Federico II) granted to G. Balassone and by the research projects CGL2016-75679-P from the Spanish Government and the Research Group RNM-179 of the Junta de Andalucìa.

REFERENCES CITED

Abad, M.M., and Nieto, F. (2003) Quantitative EDX analysis in TEM. Practical development, limitations and standards. In A. Mendez-Vilas, Ed., Science, Technology and Education of Microscopy: An Overview, p. 687-694. Badajoz, Spain, Formatex.

Arfè, G. (2018) Genesis of supergene nonsulfide zinc minerallizations in the Bongará (Peru) and Skorpion-Rosh Pinah (Namibia) areas, 266 p. PhD thesis, Università Federico II, Napoli Italy

Arfè, G., Boni, M., Mondillo, N., Aiello, R., and Balassone, G. (2016) Supergene alteration in the Capricornio Au-Ag epithermal vein system, Antofagasta Region, Chile. The Canadian Mineralogist, 54, 1-25.

Arfé, G., Mondillo, N., Balassone, G., Boni, M., Cappelletti, P., and Di Palma, T. (2017a) Identification of Zn-micas and clays from the Cristal and Mina Grande zinc deposits (Bongará Province, Amazonas Region, Northern Peru). Minerals, 7(11), 214, 1-17.

Arfè, G., Mondillo, N., Boni, M., Balassone, G., Joachimski, M., Mormone, A., and Di Palma, T. (2017b) The karst-hosted Mina Grande nonsulfide zinc deposit, Bongará district (Amazonas region, Peru). Economic Geology, 112, 1089-1110.

Arfè, G., Mondillo, N., Boni, M., Joachimski, M., Balassone, G., Mormone, A., Santoro L., and Castro Medrano E. (2018) The Cristal Zn prospect (Amazonas region, Northern Peru). Part II: An example of supergene zinc enrichments in tropical areas. Ore Geology Review, 94, 1076-1105.

Balassone, G., Nieto, F., Arfè, G., Boni, M., and Mondillo, N. (2017) Zn-clay minerals in the Skorpion Zn nonsulfide deposit (Namibia): Identification and genetic clues revealed by HRTEM and AEM study. Applied Clay Sciences, 150, 309-322.

Bauluz, B., Peacor, D.R., and González-López, J.M. (2000) Transmission electron microscopy study of illitization in pelites from the Iberian Range, Spain: layer-by-layer replacement? Clays and Clay Minerals, 48, 374–384.

Benavides-Cáceres, V. (1999) Orogenic evolution of the Peruvian Andes: the Andean Cycle. Society of Economic Geologists Special Publication 7, 61-107.

Boni, M. (2005) The geology and mineralogy of nonsulfide zinc ore deposits. In T. Fujisawa, Ed., Proceedings of Lead & Zinc ‘05 Kyoto, p. 1299–1314. Mining and Materials Processing Institute, Japan.

Boni, M., Balassone, G., Arseneau, V., and Schmidt, P. (2009a) The nonsulfide zinc deposit at Accha (Southern Peru): geological and mineralogical characterization. Economic Geology, 104, 267-289.

Boni, M., Schmidt, P.R., De Wet, J.R., Singleton, J.D. Balassone, G., and Mondillo, N. (2009b) Mineralogical signature of nonsulfide zinc ores at Accha (Peru): A key for recovery. International Journal of Mineral Processing, 93, 267-277.

Boni, M., and Mondillo, N. (2015) The "Calamines" and the "Others": the great family of supergene nonsulfide zinc ores. Ore Geology Reviews, 67, 208-233.

Borg, G., Kärner, K., Buxton, M., Armstrong, R., and Merwe, S.W. (2003) Geology of the Skorpion supergene Zn deposit, southern Namibia. Economic Geology, 98, 749-771.

695 Brigatti, M.F., and Guggenheim, S. (2002) Mica Crystal Chemistry and the influence of pressure,
696 temperature, and solid solution on atomistic models. Reviews in Mineralogy and
697 Geochemistry, 46(1), 1-97.
698 Brophy, J.A. (2012) Rio Cristal Resources Corporation Bongará zinc project. Technical Report NI
699 43-101, p. 104. Canada, Rio Cristal Resources.
700 Buatier, M., Choulet, F., Petit, S., Chassagnon, R. and Vennemann, T. (2016) Nature and origin of
701 natural Zn clay minerals from the Bou Arhous Zn ore deposit. Evidence from electron
702 microscopy (SEM-TEM) and stable isotope compositions (H and O). Applied Clay Sciences,
703 132, 377-390.
704 Choulet, F., Buatier, M., Barbanson, L., Guégan, R., and Ennaciri, A. (2016) Zinc-rich clays in
705 supergene non-sulfide zinc deposits. Mineralium Deposita, 51, 467-490.
706 Churakov, S.V., and Dähn, R. (2012) Zinc adsorption on clays inferred from atomistic simulations
707 and EXAFS spectroscopy. Environmental Science & Technology, 46, 5713–5719.
708 Cliff, G., and Lorimer, G.W. (1975) The quantitative analysis of thin specimens. Journal of
709 Microscopy, 103, 203–207.
710 Cole, P.M., and Sole, K.C. (2002) Solvent extraction in the primary and secondary processing of
711 zinc. Journal of the South African Institute of Mining and Metallurgy, 2, 451–456.
712 Dalheimer, M. (1990) The Zn-Pb-Ag deposits Huaripampa and Carahuacra in the mining district of
713 San Cristobal, central Peru, in L. Fontboté, G.C. Amstutz, M. Cardozo, E. Cedillo, E. and
714 Frutos J., Eds., Stratabound ore deposits in the Andes, p. 279-291. Springer, Berlin.
715 Einsele, G. (2000) Sedimentary basins, evolution, facies and sediment budget (2nd edition), 792 p.
716 Springer-Verlag, Berlin.
717 Emselle, N., McPhail, D.C., and Welch, S.A. (2005) Reliance, Flinders Ranges: mineralogy,
718 geochemistry and zinc dispersion around a nonsulfide orebody. In I.C. Roach, Ed.,

719 Proceedings of the CRC LEME Regional Regolith Symposia 2005, p. 86-90. CRC LEME,
720 Bentley, W.A.
721 Escamilla-Roa E., Nieto F., and Sainz-Dìaz, I. (2016) Stability of the hydronium cation in the
722 structure of illite. Clays and Clay Minerals, 64(4), 413–424.
723 Fontboté, L. (1990) Stratabound ore deposits in the Pucará basin: An overview. Society for Geology
724 Applied to Mineral Deposits Special Publication, 8, 253-266.
725 Fransolet, A.M., and Bourguignon, P. (1975) Données nouvelles sur la fraipontite de Moresnet
726 (Belgique). Bulletin de la Société Française de Minéralogie et de Cristallographie, 98, 235-
727 244.
728 Grauby, O., Petit, S., Decarreau, A., and Baronnet, A. (1993) The beidellite-saponite series: an
729 experimental approach. European Journal of Mineralogy, 5, 623-635.
730 Gu, X., and Evans, J. (2007) Modelling the absorption of Cd(II), Cu(II), Ni(II), Pb(II) and Zn(II)
731 adsorption onto Fithian illite. Journal of Colloid and Interface Science, 307, 317-325.
732 Gu, X., and Evans, J. (2008) Surface complexation modeling of Cd(II), Cu(II), Ni(II), Pb(II) and
733 Zn(II) adsorption onto kaolinite. Geochimica et Cosmochimica Acta, 72, 267–276.
734 Higashi, S., Miki, K., and Komarneni, S. (2002) Hydrothermal synthesis of Zn-smectite. Clays and
735 Clay Minerals, 50, 299-305.
736 Hitzman, M.W., Reynolds, N.A., Sangster, D.F., Allen, C.R., and Carman, C. (2003) Classification,
737 genesis, and exploration guides for nonsulfide zinc deposits. Economic Geology, 98, 685–71.
738 INGEMMET, (1995) Geologia de Los Cuadrangulos de Bagua Grande, Jumbilla, Lonya Grande,
739 Chachapoyas, Rioja, 250 Leimebamba y Bolivar. Instituto Geologico Minero y Metalurgico,
740 Boletin 56 Serie A, 390 p. Carta Geologica Nacional, Peru.
741 Kärner, K. (2006) The metallogenesis of the Skorpion Non-sulphide Zinc Deposit, Namibia.
742 Unpublished Ph.D. Thesis, Martin-Luther-Universität Halle-Wittenberg, Germany, p. 1-133.

743 Kaufhold, S., Färber, G., Dohrmann, R., Ufer, K., and Grathoff, G. (2015) Zn-rich smectite from
744 the Silver Coin Mine, Nevada, USA. Clay Minerals, 50, 417-430.
745 Kloprogge, T., Komarneni, S., and Amonette, J. (1999) Synthesis of smectite clay minerals: A
746 critical review. Clays and Clay Minerals, 47, 529-554.
747 Kobe, H.W. (1977) El Grupo Pucará y su mineralización en el Peru central: Sociedad Geologica
748 Peru Boletin, 55-56, 61-84.
749 Kobe, H.W. (1982) El ambiente de la mineralización estratoligada de Zn-Pb-Ag-Ba-Mn-Fe-Cu en
750 los sedimentos de la cuenca occidental del Pucará, Peru central. Sociedad Geologica Peru
751 Boletin, 69, 41-69.
752 Kobe, H.W. (1990a) Stratabound Cu-(Ag) deposits in the Permian Red-Bed Formation, Central
753 Peru. In L. Fontboté, G.C. Amstutz, M. Cardozo, A. Wauschkuhn, Eds., Stratabound ore
754 deposits in the Andes, p. 113-122. Berlin-Heidelberg, New York, Springer.
755 Kobe, H.W. (1990b) Metallogenic evolution of the Yauli dome, Central Peru. In L. Fontboté, G.C.
756 Amstutz, M. Cardozo, A. Wauschkuhn, Eds., Stratabound ore deposits in the Andes, p. 267-
757 278. Berlin-Heidelberg, New York, Springer.
758 Large, D. (2001) The geology of non-sulphide zinc deposits - An overview. Erzmetall 54, 264–276.
759 Lozano, R.P., Rossi, C., La Iglesia, Á., and Matesanz, E. (2012) Zaccagnaite-3R, a new Zn-Al
760 hydrotalcite polytype from El Soplao cave (Cantabria, Spain). American Mineralogist, 97,
761 513-523.
762 Mills, S.J., Christy, A.G., Genin, J.-M.R., Kameda, T., and Colombo, F. (2012) Nomenclature of
763 the hydrotalcite supergroup: natural layered double hydroxides. Mineralogical Magazine, 76,
764 1289-1336.
765 Manceau, A., Lanson, B., Schlegel, M.L., Harge, J.C., Musso, M., Eybert-Berard, L., Hazemann,
766 J.L., Chateigner, D., and Lamble, G.M. (2000) Quantitative Zn speciation in smelter-
767 contaminated soils by EXAFS spectroscopy. American Journal of Sciences, 300, 289-343.

768 Mégard, F. (1984) The Andean Orogenic Period and its major structures in central and northern
769 Peru. Journal of the Geological Society, 141, 893-900.
770 Mégard, F. (1987) Structures and evolution of the Peruvian Andes. In J. Schaer and J. Rodgers,
771 Eds., The anatomy of mountain ranges, p. 179-210. Princeton University Press, Princeton, NJ.
772 Merriman, R.J., and Peacor, D.R. (1999) Very low-grade metapelites: mineralogy, microfabrics and
773 measuring reaction progress. In: M. Frey and D. Robinson, Eds., Low-grade metamorphism,
774 p. 12-87. Blackwell Science, Oxford.
775 Meunier, A. (2005) Clays, p. 472. Springer Verlag, Berlin.
776 Meunier, A., and Velde, B. (2004) Illite, p. 286. Springer, Berlin.
777 Mondillo, N., Boni, M., Balassone, G., and Villa, I.M. (2014) The Yanque Prospect (Peru): From
778 Polymetallic Zn-Pb Mineralization to a Nonsulfide Deposit. Economic Geology, 109, 1735-
779 1762.
780 Mondillo, N., Nieto, F., and Balassone, G. (2015) Micro- and nano-characterization of Zn-clays in
781 nonsulfide supergene ores of southern Peru. American Mineralogist, 100, 2484-2496.
782 Mondillo, N., Arfè, G., Boni, M., Balassone, G., Boyce, A., Joachimski, M., and Villa, I.M. (2018a)
783 The Cristal Zn prospect (Amazonas region, Northern Peru), Part I: New insights on the sulfide
784 mineralization in the Bongará province. Ore Geology Review, 94, 261-276.
785 Mondillo, N., Arfè, G., Herrington, R., Boni, M., Wilkinson, C., and Mormone, A. (2018b)
786 Enrichments of Ge in supergene settings: Evidence from the Cristal supergene Zn nonsulfide
787 prospect, Bongará district, Northern Peru. Mineralium Deposita, 53(2), 155-169.
788 Montoya, V., Baeyens, B., Glaus, M.A., Kupcik, T., Marques Fernandes, M., Van Laer, L.,
789 Bruggeman, C., Maes, N., and Schäfer, T. (2018) Sorption of Sr, Co and Zn on illite: Batch
790 experiments and modelling including Co in-diffusion measurements on compacted samples.
791 Geochimica et Cosmochimica Acta, 223, 1-20.

792 Moore, D.M., and Reynolds, R.C.J. (1997) X-ray diffraction and the identification and analysis of
793 clay minerals, p. 378. Oxford University Press, New York.
794 Newman, A.C.D., and Brown, G. (1987) The chemical constitution of clays. In A.C.D. Newman,
795 Ed., Chemistry of Clays and Clay Minerals, p. 128. John Wiley & Sons, New York.
796 Nieto, F., Ortega-Huertas, M., Peacor, D.R., and Aróstegui, J. (1996) Evolution of illite/smectite
797 from early diagenesis through incipient metamorphism in sediments of the Basque-Cantabrian
798 basin. Clays and Clay Minerals. 44, 304–323.
799 Nieto, F., Mellini, F., and Abad, I. (2010) The role of H_3O^+ in the crystal structure of illite. Clays
800 and Clay Minerals, 58(2), 238–246.
801 Paradis, S., Hannigan, P., and Dewing, K. (2007) Mississippi Valley-type lead-zinc deposits. In
802 Goodfellow, W.D., Ed., Mineral deposits of Canada: A synthesis of major deposit-types,
803 district metallogeny, the evolution of geological provinces, and exploration methods, p. 185-
804 203. Geological Association of Canada, Mineral Deposits Division, Special Publication No.
805 5, St. John's, NL, Canada.
806 Pascua, C.S., Ohnuma, M., Matsushita, Y., Tamura, K., Yamada, H., Cuadros, and J., Ye, J. (2010)
807 Synthesis of monodisperse Zn-smectite. Applied Clay Science, 48, 55-59.
808 Petit, S., Righi, D., and Decarreau, A. (2008) Transformation of synthetic Zn-stevensite to Zn-talc
809 induced by the Hofmann-Klemen effect. Clays and Clay Minerals, 56, 645-654.
810 Reid, C.J. (2001) Stratigraphy and mineralization of the Bongará MVT zinc-lead district, northern
811 Peru, p. 179. M.Sc. thesis, University of Toronto, Canada.
812 Rieder, M., Cavazzini, G., D'Yakonov, Y.S., Kamanetskii, V.A.F., Gottardi, G., Guggenheim, S.,
813 Koval, P.K., Muller, G., Neiva, A.M.R., Radoslovich, E.W., Robert, J.L., Sassi, F.P., Takeda,
814 H., Weiss, Z., and Wones, D.R. (1998) Nomenclature of the micas. The Canadian
815 Mineralogist, 36, 1-8.

816 Robert, J.L., and Gaspérin, M. (1985) Crystal structure refinement of hendricksite, A Zn- and Mn-
817 rich trioctahedral potassium mica: A contribution to the crystal chemistry of zinc-bearing
818 minerals. Mineralogy and Petrology, 34, 1-14.
819 Rosas, S., Fontboté, L., and Tankard, A. (2007) Tectonic evolution and paleogeography of the
820 Mesozoic Pucará basin, central Peru. Journal of South American Earth Sciences, 24, 1-24.
821 Ross, C.S. (1946) Sauconite - a clay mineral of the Montmorillonite group. American Mineralogist,
822 31, 411-424.
823 Rule, A.C., and Radke, F. (1988) Baileychlore, the Zn end member of the trioctahedral chlorite
824 series. American Mineralogist, 73, 135-139.
825 Sharygin, V.V. (2015) Zincian micas from peralkaline phonolites of the Oktyabrsky massif, Azov
826 Sea region, Ukrainian Shield. European Journal of Mineralogy, 4, 521-533.
827 Srivastava, P., Singh, B., and Angove, M. (2005) Competitive adsorption behavior of heavy metals
828 on kaolinite. Journal of Colloid and Interface Science, 290, 28–38.
829 Środon, J., and Eberl, D.D. (1984) Illite. In: S.W. Bailey (Ed.), Micas, 13, p. 495-544. Reviews in
830 Mineralogy and Geochemistry, Mineralogical Society of America, Chantilly, Virginia.
831 Vázquez, M., Nieto, F., Morata, D., Droguet, B., Cariili-Rosua, F.J., and Morales, S. (2014)
832 Evolution of clay mineral assemblages in the Tinguiririca geothernal field, Andean Cordillera
833 of central Chile: an XRD and HRTEM-AEM study. Journal of Volcanology and Geothermal
834 Research, 282, 43-59.
835 Vázquez, M., Bauluz, B., Nieto, F., and Morata, D. (2016) Illitization sequence controller by
836 temperature in volcanic geothermal system: the Tinguiririnca geothermal field, Andean
837 Coridllera, Central Chile. Applied Clay Science, 134, 221-234.
838 Whitney, D. L., and Evans, B. W. (2010) Abbreviations for names of rock-forming minerals.
839 American Mineralogist, 95, 185–187.

Will, P., Friedrich, F., Hochleitner, R., and Gilg, H.A. (2014) Fraipontite in the hydrothermally overprinted oxidation zone of the Preguiça mine, Southern Portugal. Abstract Mid-European Clay Conference, 16-19 September 2014, Dresden, Germany.

Wright, C. (2010) Rio Cristal Resources Corporation Bongará Zinc Project: Technical Report NI 43-101, p. 102. Canada, Rio Cristal Resources Corporation and AMEC, Peru.

Yamada, H.,Yoshioka, K.,Tamura, K., Fujii, K., and Nakazawa, H. (1999) Compositional gap in dioctahedral-trioctahedral smectite system: beidellite-saponite pseudo-binary join. Clays and Clay Minerals, 47, 803-810.

Zhang, C., He, H. Tao, Q., Ji, S., Li, S., Ma, L., Su, X., and Zhu, J. (2017) Metal occupancy and its influence on thermal stability of synthetic saponites. Applied Clay Science, 135, 282–288.

LIST OF FIGURES CAPTIONS

FIGURE 1. (a) Geological map of the Bongará district within the Northern Andes morphostructural units B (modified from Arfè et al. 2017b), with location of Mina Grande and Cristal ore fields. (b) Stratigraphic column of the succession in the Bongará area (modified from Brophy 2012).

FIGURE 2. The studied samples from the nonsulfide Mina Grande and Cristal zinc deposits, Bongará (Peru), scale bar is equal to 2 cm.

FIGURE 3. Sample ZB-1 (Mina Grande): (a) textural images of Zn-illite (Zn-Ilt), with fraipontite (Frp). (b) HRTEM image of Zn-Illite in the yellow frame in the image (a), corresponding to a basically disordered polytype, with misorientation among the packets typical of illite (or I3 I/S

mixed-layer); the SAED in the inset shows the [100] pattern with reflections (00l) at 10 Å of MDT Zn-illite and 9 Å average period in the b* direction. Rows corresponding to (02l) and (04l) are basically ill-defined diffuse lines, typical of disordered polytypes. (c) HRTEM of another area in yellow circle of (a), with the white fringes likely corresponding to a I3 I/S mixed layer. FFT (inset) shows the misorientation among the layers of the various packets and spacing which correspond to c*, b* and a* of illite and c* of the I3 I/S (4 illite + 1 smectite layers, in crimson). (d) HRTEM image of fraipontite close to Zn-illite, indicated by the sky-blue circle of image (a). (e) Chemical map of Zn-illite (Zn-Ilt), fraipontite and Fe-Ti-oxides (Fe-ox, Ti-ox) of a different zone from the previous ones, with the EDX spectrum referring to Zn-illite of the white frame area. Hereafter the Cu peak visible in the EDX spectra comes from to the copper ring used for TEM sample preparation (mineral abbreviations mainly in agreement with Whitney and Evans 2010).

FIGURE 4. (a) Textural image of an area in Sample ZB-1 formed by MDT Zn-illite only (MDT Zn-Ilt, see text for acronym explanation); in the inset, SAED [100] + [010] patterns of illite (c* = 10Å, a* = 5.2 Å and b* = 9 Å) related to the yellow circle area; (02l), (20l) and (04l) rows are continuous diffuse lines, typical of disordered polytypes. (b) Sample ZB-1, MDT Zn-illite with fraipontite (Frp) and Fe,Ti oxide (Fe-ox, Ti-ox). (c) Sample ZB-2, smooth transition zone of MDT Zn-illite/fraipontite; the inset reports the electron diffraction pattern mainly taken in the left side of the investigated area, displaying rows with the fraipontite (7 Å) and illite (10Å) spacing, in parallel orientation (see text). (d) Sample ZB-1, chemical map of MDT Zn-illite of a different zone from those reported in (a) and (b), with Fe,Ti(Mn) oxide and fraipontite. (e) STEM-EDX spectra 1 and 2 of MDT Zn-illite and fraipontite in image (d).

FIGURE 5. Sample ZB-2 (Mina Grande): (a) textural and (b) chemical map of a zinc illite area (both MDT Zn-Ilt and Zn-Ilt, see text for further explanation), with fraipontite (Frp), kaolinite (Kln), Fe-(hydr)oxides (Fe-ox) and rutile (Ti-ox); the top right inset shows the lattice fringes of the zinc illite area in the white circle. (c) Selected chemical maps (K, Zn and Mg) of the investigated site in (a) and (b). (d) Qualitative EDX spectra of the two areas indicated in image (b). Images a, b and c show the intergrowth between the trioctahedral and dioctahedral micas at the ~20 nm scale.

FIGURE 6. Sample ZB-2: (a) Particles deposited onto a copper grid (CM20 instrument), showing Zn-illite (Zn-Ilt), K-deficient hendricksite (Hnk, see text for explanation), fraipontite (Frp) and Fe(Mn)-oxi-hydroxides (Fe,Mn-ox). (b) Qualitative EDX spectra of K-deficient hendricksite and fraipontite, related to the areas in the red frames of image (a).

FIGURE 7. Sample ZB-2: (a) HAADF and (b) chemical map image of a fraipontite-rich area, with a possible replacement by zaccagnaite (in the dashed areas); see in particular the C peak in the EDX spectrum. (c) Si distribution in image (b).

FIGURE 8. Sample CR07-13 (Cristal): (a) chemical map of Zn-illite (Zn-Ilt) of, with typical differences of composition among the packets. (b) HRTEM and SAED patterns of Zn-bearing illite (black circle area in image a), showing a periodicity of 10 Å. (c) Qualitative EDX spectra of two chemically different areas of Zn-bearing illite in image (a).

FIGURE 9. (a) The Zn-illite-rich area of sample CR07-13, showing differences of orientation among the various packets; SAED in the inset, corresponding to the yellow circle area, shows rows (00l) with spacing equal to 10 Å, and the row (02l) showing 20 Å periodicity, characteristic of 2M

polytype; in addition to [100], other orientations from different packets are also visible in the SAED (b) Another area with prevailing Zn-illite; the left SAED (yellow circle) corresponds to a disordered polytype in [100] orientation, whereas the right one (white circle) includes both rows corresponding to [010] orientation, with a periodicity of 10 Å and to [100] with 20 Å periodicity, characteristic of 2M polytype. (c) HRTEM image of interstratified I/S type, with minor proportion of smectite layers (I3). (d) HRTEM images of Zn-illite, with small disoriented packets.

FIGURE 10. Sample CR13-7 (Cristal): (a) chemical map of Zn-illite (blue areas) interleaved with smectite, corresponding to Zn-bearing beidellite (Bdl, the red areas and related EDX spectrum), and montmorillonite (Mnt); the HRTEM (white circle) demonstrates the occurrence both of smectite and illite. Hemimorphite (Hem) and Fe-(hydr)oxides (Fe-ox) also occur in the investigated area. (b) Chemical map of another zone in the same sample, showing Zn-illite with sauconite (Sau, see also the EDX spectrum) and monazite (Mnz).

FIGURE 11. Bivariate plots of (a) Al_{tot} vs. Si, (b) Zn vs. Al^{VI} and (c) Zn vs. K, expressed in terms of atoms per formula units (apfu), illustrating the compositional variations of clay minerals from Mina Grande and Cristal deposits (point-analyses with bold line refer to compositions approaching Zn-bearing muscovite, see Tables 4 and 5).

FIGURE 12. (a) $4Si\text{-}M^{+}\text{-}3R^{2+}$ diagram, showing the compositional variations of di- and trioctahedral phyllosilicates of the Bongará samples. The top left inset illustrates selected literature data: ideal muscovite (M), hendricksite (H), sauconite (S), beidellite (B), kaolinite (K) and fraipontite (F) compositions; black line refers to mica, fraipontite and sauconite compositional fields from supergene Zn ores of Bou Arhous, Morocco (Choulet et al. 2016); red line fields are related to

939 sauconite, beidellite and muscovite from Skorpion, Namibia (Balassone et al. 2017); blue line
940 fields are referred to beidellite (left) and sauconite (center) compositions from Peru (Mondillo et
941 al. 2016). (b) Schematic compositional fields of Zn-bearing phyllosilicates of Mina Grande and
942 Cristal in the K-Zn-Al^{VI} system. The top left inset shows compositions of ideal compositions of
943 muscovite (M), hendricksite (H) and fraipontite (F) plotted in the same diagram (from IMA
944 database and Mondillo et al. 2018, and references therein) (point-analyses with bold line as in
945 Fig. 11).
946
947 **FIGURE 13.** Chemical mappings of the typical infiltration of Fe-Mn (hydr)oxides in zinc silicates at
948 very fine scale: (a) Fe(Mn)-ox (mainly Mn-bearing goethite) with Zn-illite (Zn-Ilt); (b)
949 chalcophanite with hemimorphite (sample CR13-7).
950
951
952 **LIST OF TABLES CAPTIONS**
953
954 **Table 1.** Theoretical formulae of Zn-bearing phyllosilicates and other selected minerals cited in the
955 text (IMA database, http://rruff.info/ima/).
956
957 **Table 2.** Selected structural formulae of phyllosilicates from sample ZB-1, in atoms per formula
958 units (apfu), calculated on the basis of 11 oxygens for MDT Zn-illite and K-deficient
959 hendricksite, 6 octahedral+tetrahedral cations for Zn-illite (as in Nieto et al. 2010) and 7 oxygens
960 for fraipontite.
961
962 **Table 3.** Selected structural formulae of phyllosilicates from sample ZB-2, in atoms per formula
963 units (apfu), calculated on the basis of 11 oxygens for MDT Zn-illite and K-deficient

964 hendricksite, 6 octahedral+tetrahedral cations for Zn-illite (as in Nieto et al. 2010) and 7 oxygens
965 for fraipontite and kaolinite.
966
967 **Table 4.** Selected structural formulae of phyllosilicates from sample CR07-13, in atoms per formula
968 units (apfu), calculated on the basis of 11 oxygens for Zn-illite MDT and 6
969 octahedral+tetrahedral cations for Zn-illite and muscovite (as in Nieto et al. 2010).
970
971 **Table 5.** Selected structural formulae of phyllosilicates from sample CR13-7, in atoms per formula
972 units (apfu), calculated on the basis of 11 oxygens for Zn-bearing illite MDT, sauconite,
973 beidellite and montmorillonite and 6 octahedral+tetrahedral cations for Zn-bearing illite and
974 muscovite (as in Nieto et al. 2010).
975
976
977

Table 1. Theoretical formulae of Zn-bearing phyllosilicates and other selected minerals cited in the text (IMA database, http://rruff.info/ima/)

Mineral	Ideal formula
Beidellite	$(Na,Ca)_{0.3}Al_2(Si,Al)_4O_{10}(OH)_2 \cdot n(H_2O)$
Chalcophanite	$ZnMn^{4+}{}_3O_7 \cdot 3H_2O$
Fraipontite	$(Zn,Al)_3(Si,Al)_2O_5(OH)_4$
Goethite	$FeO(OH)$
Hemimorphite	$Zn_4Si_2O_7(OH)_2 \cdot (H_2O)$
Hendricksite	$KZn_3(Si_3Al)O_{10}(OH)_2$
Hydrozincite	$Zn_5(CO_3)_2(OH)_6$
Illite*	$(K,H_3O)(Al,Mg,Fe)_2(Si, Al)_4O_{10}[(OH)_2,(H_2O)]$
Kaolinite	$Al_2Si_2O_5(OH)_4$
Montmorillonite	$(Na,Ca)_{0.3}(Al,Mg)_2Si_4O_{10}(OH)_2 \cdot nH_2O$
Muscovite	$KAl_2(Si_3Al)O_{10}(OH)_2$
Sauconite	$Na_{0.3}Zn_3(Si,Al)_4O_{10}(OH)_2 \cdot 4H_2O$
Smithsonite	$ZnCO_3$
Zaccagnaite	$Zn_4Al_2(OH)_{12}(CO_3) \cdot 3(H_2O)$

Notes: *From http://www.webmineral.com/

Table 2. Selected structural formulae of phyllosilicates from sample ZB-1, in atoms per formula units (apfu), calculated on the basis of 11 oxygens for MDT Zn-illite and K-deficient hendricksite, 6 octahedral+tetrahedral cations for Zn-illite (as in Nieto et al. 2010) and 7 oxygens for fraipontite

mineral	Zn-illite	MDT Zn-illite	MDT Zn-illite	MDT Zn-illite	MDT Zn-illite	MDT Zn-illite	MDT Zn-illite	MDT Zn-illite	K-deficient hendricksite	K-deficient hendricksite	fraipontite	fraipontite	fraipontite	fraipontite	fraipontite
analysis ref. #	3.cuan-MAP 3	anl. 1	2.cuan-MAP1	3.cuan-MAP1	4.cuan-MAP1	6.cuan-MAP1	7.cuan-MAP1	2.cuan-MAP 2	anl. 2	anl. 4	3.cuan-MAP 2	1.cuan-MAP 3	2.cuan-MAP 3	anl. 3	anl. 5
Si	3.06	3.17	2.85	2.57	2.95	2.69	2.63	3.14	2.87	2.92	1.10	1.08	1.11	1.21	1.35
Al^{IV}	0.94	0.83	1.15	1.43	1.05	1.31	1.37	0.86	1.13	1.08	0.90	0.92	0.89	0.79	0.65
Al^{VI}	1.31	1.08	0.90	0.56	0.89	0.43	0.56	1.29	0.88	0.86	0.36	0.39	0.30	0.46	0.57
Ti	0.03	-	0.41	0.52	0.32	0.45	0.41	-	-	-	-	-	-	-	-
Mg	0.26	0.22	0.31	0.36	0.46	0.32	0.29	0.21	0.22	0.24	-	-	-	-	-
Fe	-	0.20	0.46	0.81	0.39	1.06	0.43	0.04	0.13	0.20	0.04	0.05	0.04	0.16	0.16
Zn	0.40	0.92	0.32	0.29	0.38	0.30	0.96	0.88	1.55	1.55	2.86	2.82	2.96	2.56	2.33
$\Sigma_{octahedral}$	2.00	2.42	2.40	2.53	2.43	2.57	2.65	2.42	2.78	2.84	3.26	3.26	3.30	3.17	3.05
K	0.75	0.90	0.48	0.54	0.55	0.52	0.56	0.74	0.70	0.57	-	-	-	-	-

Note: - below detection limit

Table 3. Selected structural formulae of phyllosilicates from sample ZB-2, in atoms per formula units (apfu), calculated on the basis of 11 oxygens for MDT Zn-illite and K-deficient hendricksite. 6 octahedral+tetrahedral cations for Zn-illite (as in Nieto et al. 2010) and 7 oxygens for fraipontite and kaolinite

mineral	Zn-illite	Zn-illite MDT	MDT Zn-illite	MDT Zn-illite	MDT Zn-illite	K-deficient hendricksite	fraipontite	fraipontite	fraipontite	fraipontite	fraipontite	kaolinite	kaolinite
analysis ref. #	6.cuan-MAP 1	3.cuan-MAP 1	anl. 2	spc 3430	2.cuan-MAP 1	anl. 1	anl. 4	anl. 6	anl. 7	4.cuan-MAP 1	7.cuan-MAP 1	8.cuan-MAP 1	spc 3421
Si	3.14	2.93	3.10	2.80	3.09	2.87	1.30	1.17	1.40	1.34	1.27	2.10	2.00
Al^{IV}	0.86	1.07	0.90	1.20	0.91	1.13	0.70	0.83	0.60	0.66	0.66	0.00	0.00
Al^{VI}	1.49	1.14	1.03	0.83	1.42	0.83	0.56	0.34	0.67	0.62	0.68	1.66	1.41
Ti	-	-	-	0.06	-	-	-	-	-	-	-	-	-
Mg	0.19	0.20	0.18	0.15	0.20	-	-	-	-	-	-	0.13	0.13
Fe	0.01	0.05	-	0.59	0.09	0.13	0.14	0.10	0.11	0.07	0.10	0.00	0.00
Zn	0.31	1.28	1.44	1.09	0.65	1.89	2.35	2.81	2.19	2.32	2.22	0.12	0.70
$\Sigma_{octahedral}$	2.00	2.67	2.65	2.73	2.36	2.84	3.06	3.25	2.97	3.01	3.01	1.91	2.24
K	0.70	0.57	0.55	0.63	0.74	0.65	-	-	-	-	-	0.14	0.12

Note: - below detection limit

Table 4. Selected structural formulae of phyllosilicates from sample CR07-13, in atoms per formula units (apfu), calculated on the basis of 11 oxygens for Zn-illite MDT and 6 octahedral+tetrahedral cations for Zn-illite and muscovite (as in Nieto et al. 2010)

mineral	Zn-muscovite	Zn-muscovite	Zn-illite	Zn-illite	Zn-illite	Zn-illite	Zn-muscovite	Zn-illite	Zn-illite	MDT Zn-illite
analysis ref. #	anl. 5	anl. 11	1.cuan-MAP 1	2.cua -MAP 1	3.cuan-MAP 1	4.cuan-MAP 1	1.cuan-MAP 2	7.cuan-MAP 2	spc 3399	anl. 2
Si	3.29	3.04	3.29	3.18	3.18	3.21	2.89	3.57	3.25	2.93
Al^{IV}	0.71	0.96	0.71	0.82	0.82	0.79	1.11	0.43	0.75	1.07
Al^{VI}	1.30	1.24	1.45	1.50	1.45	1.41	0.90	1.17	1.43	0.60
Ti	-	-	-	-	-	-	-	-	-	-
Mg	0.25	-	0.26	0.22	0.32	0.25	0.17	0.60	0.27	0.26
Fe	0.38	-	0.21	0.10	0.19	0.13	0.84	0.19	0.24	0.69
Mn	-	0.65	-	-	-	-	-	-	-	0.98
Zn	0.07	0.11	0.08	0.18	0.04	0.21	0.09	0.04	0.05	0.39
$\Sigma_{octahedral}$	2.00	2.00	2.00	2.00	2.00	2.00	2.00	2.00	2.00	2.92
K	1.07	1.01	0.72	0.67	0.67	0.53	0.81	0.56	0.73	0.65

Note: - below detection limit

Table 5. Selected structural formulae of phyllosilicates from sample CR13-7, in atoms per formula units (apfu), calculated on the basis of 11 oxygens for MDT Zn-illite, sauconite, beidellite and montmorillonite and 6 octahedral+tetrahedral cations for Zn-illite and muscovite (as in Nieto et al. 2010)

mineral	Zn-illite	Zn-illite	Zn-muscovite	Zn-illite	Zn-illite	Zn-illite	Zn-illite	Zn-muscovite	MDT Zn-illite	MDT Zn-illite	sauconite	sauconite	beidellite	montomorillonite
analysis ref. #	6.cuan MAP 3	7.cuan-MAP 3	3.cuan-MAP 4	3.cuan-MAP 5	4.cuan-MAP 5	9.cuan-MAP 5	10.cuan-MAP 5	11.cuan-MAP 5	anl. 5	anl. 7	anl. 2	2.cuan-MAP 3	6.cuan-MAP 5	8.cuan-MAP 5
Si	3.48	3.58	3.36	3.38	3.26	3.31	3.66	3.39	2.73	2.67	2.64	4.11	3.70	4.01
Al^{IV}	0.52	0.42	0.64	0.62	0.74	0.69	0.34	0.61	1.27	1.33	1.36	0.00	0.30	0.00
Al^{VI}	1.64	1.77	1.37	1.64	1.41	1.67	1.44	1.66	0.51	0.51	0.00	0.31	1.81	1.60
Ti	-	-	-	-	0.04	-	-	-	-	-	-	0.05	-	-
Mg	0.29	0.16	0.29	0.32	0.32	0.23	0.27	0.21	-	-	0.23	-	0.24	0.16
Fe	0.03	-	0.19	0.03	0.16	0.04	0.01	0.03	1.07	0.81	0.13	-	0.05	0.10
Mn	-	-	-	-	-	-	-	-	0.28	0.90	0.66	-	-	-
Zn	0.04	0.07	0.15	0.02	0.08	0.06	0.27	0.10	0.86	0.71	2.58	2.09	0.02	0.14
$\Sigma_{octahedral}$	2.00	2.00	2.00	2.00	2.00	2.00	2.00	2.00	2.72	2.93	3.55	2.46	2.12	2.09
K	0.62	0.67	0.94	0.56	0.72	0.58	0.34	0.91	0.88	0.80	0.32	0.23	0.19	0.03

Note: - below detection limit

a

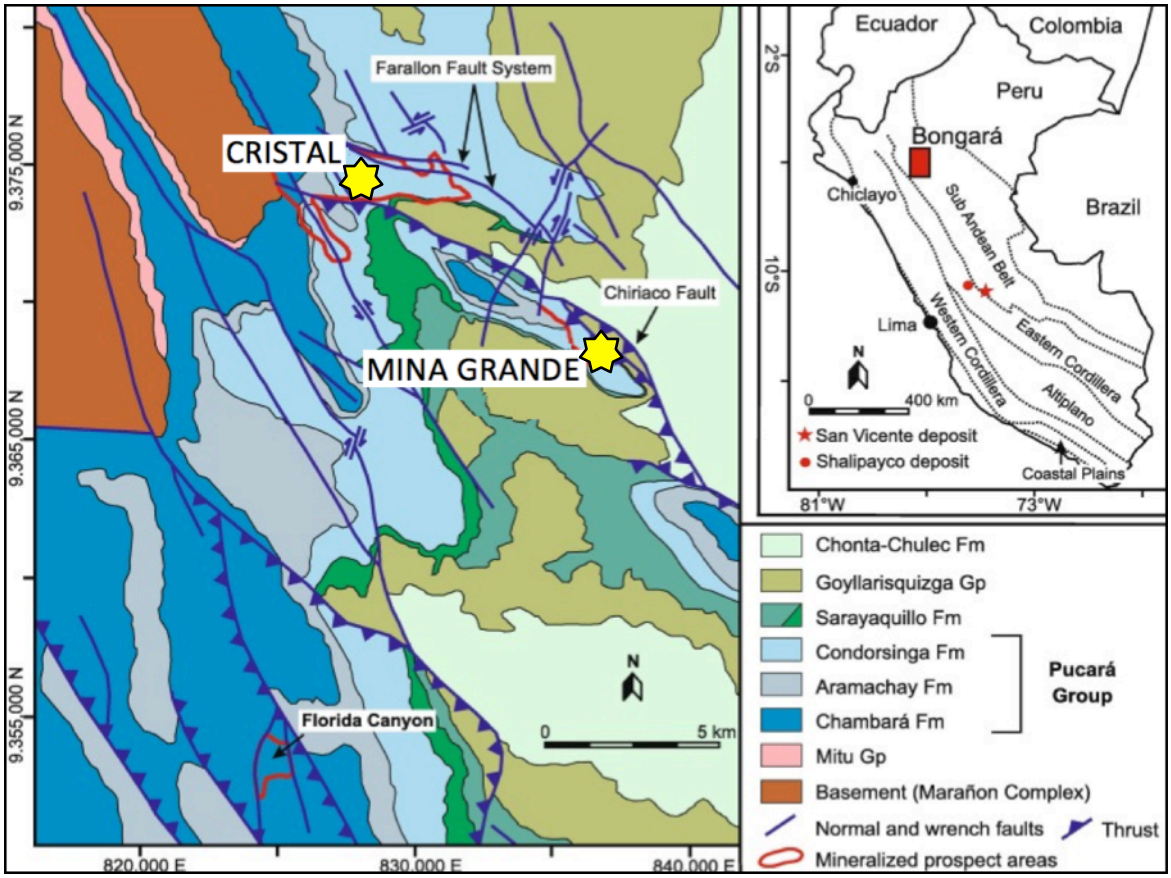
Farallon Fault System
CRISTAL
Chiriaco Fault
MINA GRANDE
Florida Canyon
N
0
5 km
9.375,000 N
9.365,000 N
9.355,000 N
820,000 E
830,000 E
840,000 E
Ecuador
Colombia
Peru
Bongará
Chiclayo
Brazil
Sub Andean Belt
Lima
Western Cordillera
Eastern Cordillera
Altiplano
Coastal Plains
400 km
San Vicente deposit
Shalipayco deposit
2°S
10°S
81°W
73°W
Chonta-Chulec Fm
Goyllarisquizga Gp
Sarayaquillo Fm
Condorsinga Fm
Aramachay Fm
Chambará Fm
Pucará Group
Mitu Gp
Basement (Marañon Complex)
Normal and wrench faults
Thrust
Mineralized prospect areas

b

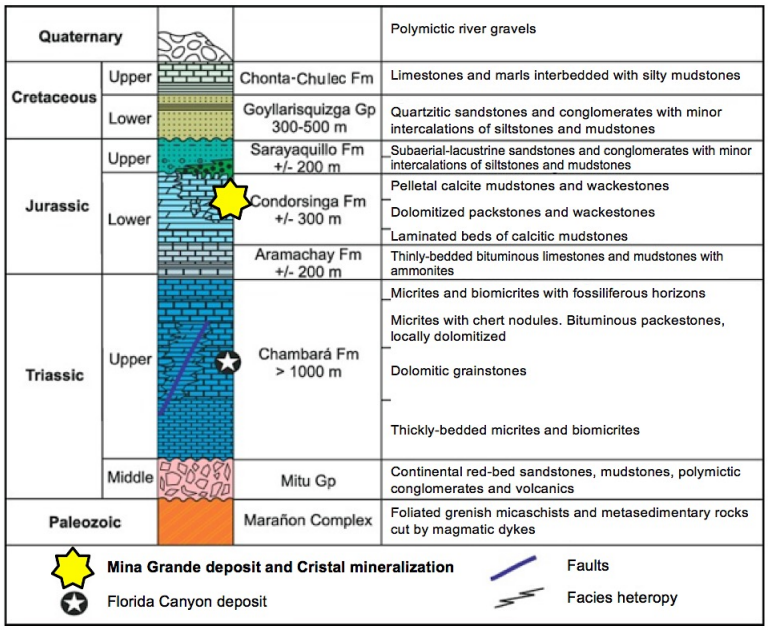
Quaternary
Polymictic river gravels
Cretaceous
Upper
Chonta-Chulec Fm
Limestones and marls interbedded with silty mudstones
Lower
Goyllarisquizga Gp 300-500 m
Quartzitic sandstones and conglomerates with minor intercalations of siltstones and mudstones
Jurassic
Upper
Sarayaquillo Fm +/- 200 m
Subaerial-lacustrine sandstones and conglomerates with minor intercalations of siltstones and mudstones
Lower
Condorsinga Fm +/- 300 m
Pelletal calcite mudstones and wackestones
Dolomitized packstones and wackestones
Laminated beds of calcitic mudstones
Aramachay Fm +/- 200 m
Thinly-bedded bituminous limestones and mudstones with ammonites
Triassic
Upper
Chambará Fm > 1000 m
Micrites and biomicrites with fossiliferous horizons
Micrites with chert nodules. Bituminous packestones, locally dolomitized
Dolomitic grainstones
Thickly-bedded micrites and biomicrites
Middle
Mitu Gp
Continental red-bed sandstones, mudstones, polymictic conglomerates and volcanics
Paleozoic
Marañon Complex
Foliated grenish micaschists and metasedimentary rocks cut by magmatic dykes
Mina Grande deposit and Cristal mineralization
Florida Canyon deposit
Faults
Facies heteropy

FIGURE 1

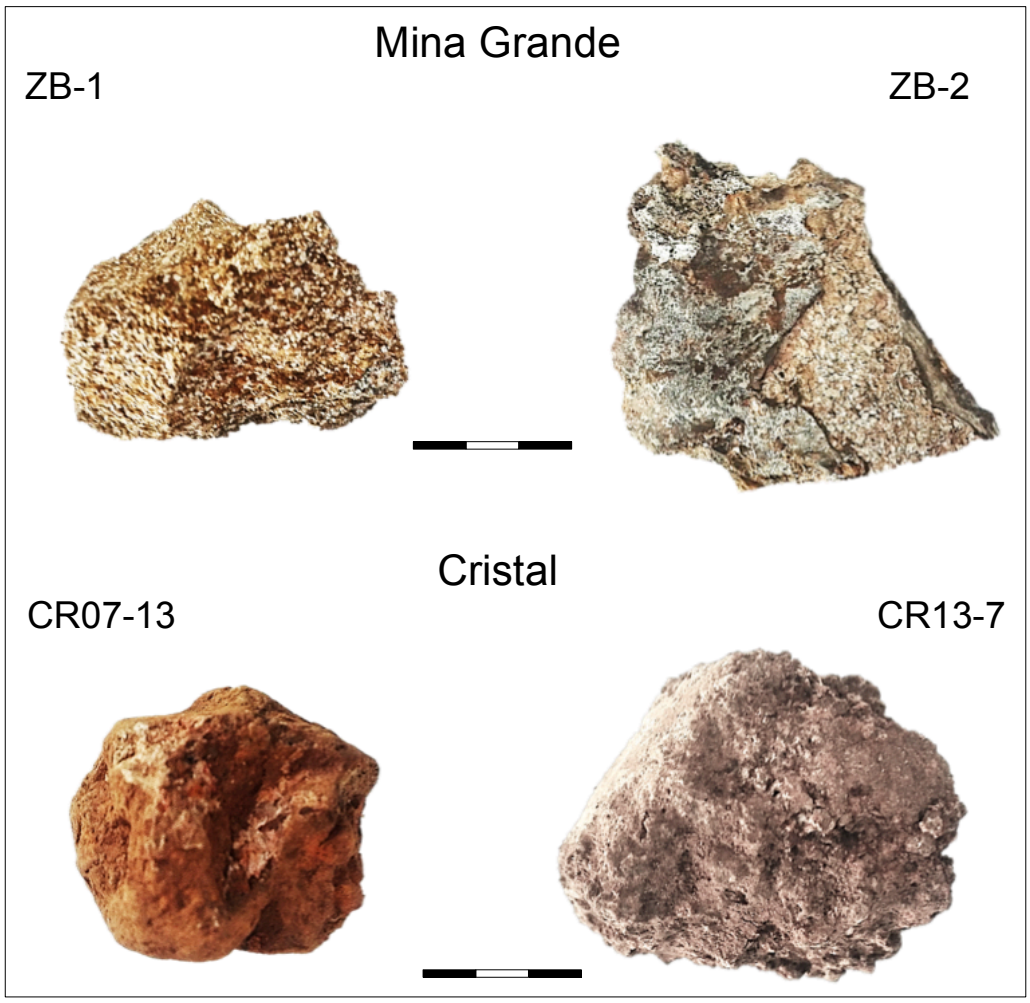

FIGURE 2

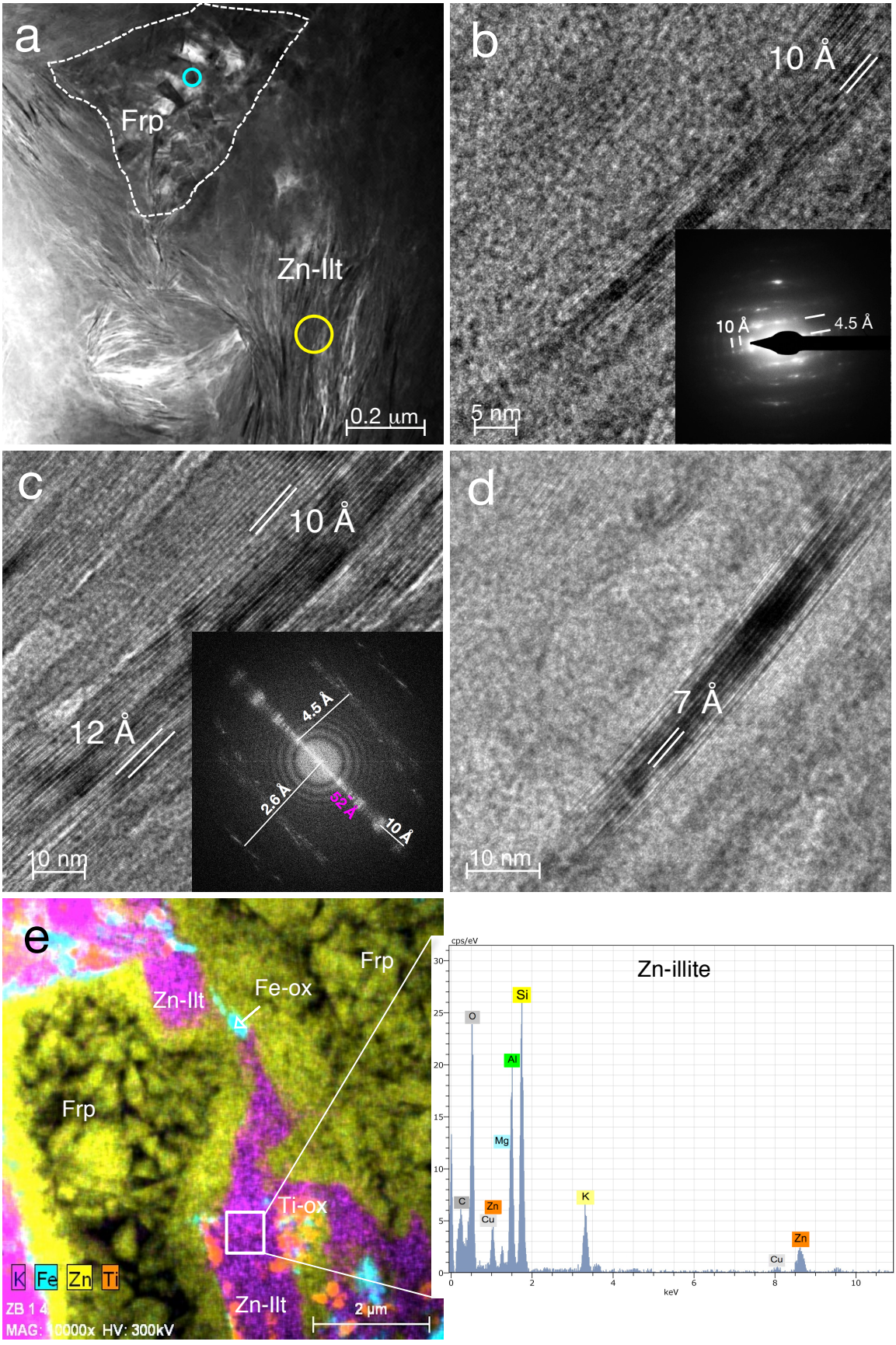
a
Frp
Zn-Ilt
0.2 µm
b
10 Å
10 Å
4.5 Å
5 nm
c
10 Å
12 Å
4.5 Å
2.6 Å
10 Å
10 nm
d
7 Å
10 nm
e
Frp
Zn-Ilt
Fe-ox
Frp
Ti-ox
Zn-Ilt
K Fe Zn Ti
ZB 1 4
MAG: 10000x HV: 300kV
2 µm
cps/eV
Zn-illite
O
Si
Al
Mg
C
Zn
Cu
K
Zn
Cu
keV

FIGURE 3

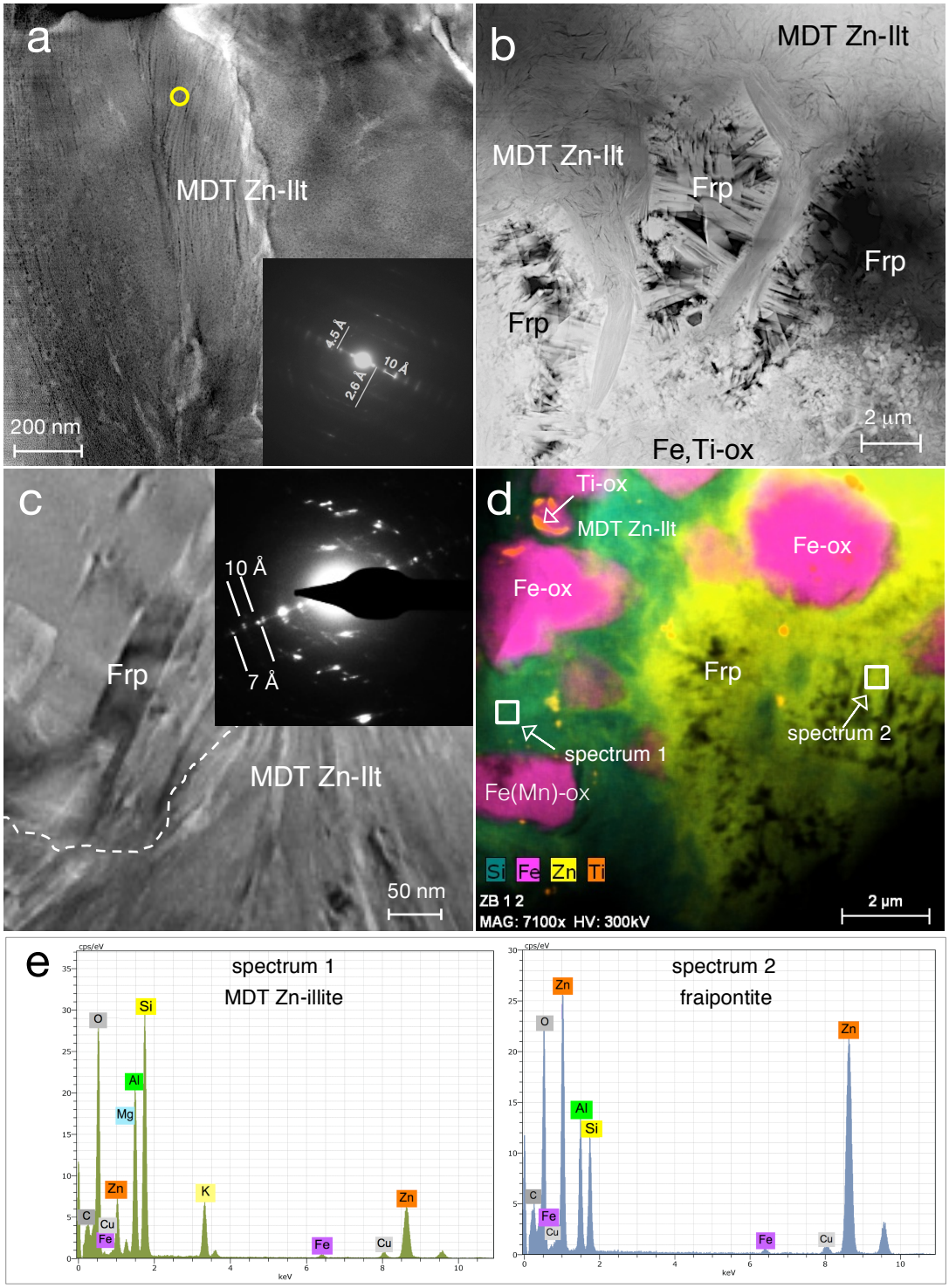
a
MDT Zn-Ilt
4.5 Å
10 Å
2.6 Å
200 nm
b
MDT Zn-Ilt
MDT Zn-Ilt
Frp
Frp
Frp
Fe,Ti-ox
2 µm
c
Frp
10 Å
7 Å
MDT Zn-Ilt
50 nm
d
Ti-ox
MDT Zn-Ilt
Fe-ox
Fe-ox
Frp
spectrum 1
spectrum 2
Fe(Mn)-ox
Si Fe Zn Ti
ZB 1 2
MAG: 7100x HV: 300kV
2 µm
e
spectrum 1
MDT Zn-illite
cps/eV
O
Si
Al
Mg
Zn
K
C
Cu
Fe
Fe
Cu
Zn
keV
spectrum 2
fraipontite
cps/eV
Zn
O
Zn
Al
Si
C
Fe
Cu
Fe
Cu
keV

FIGURE 4

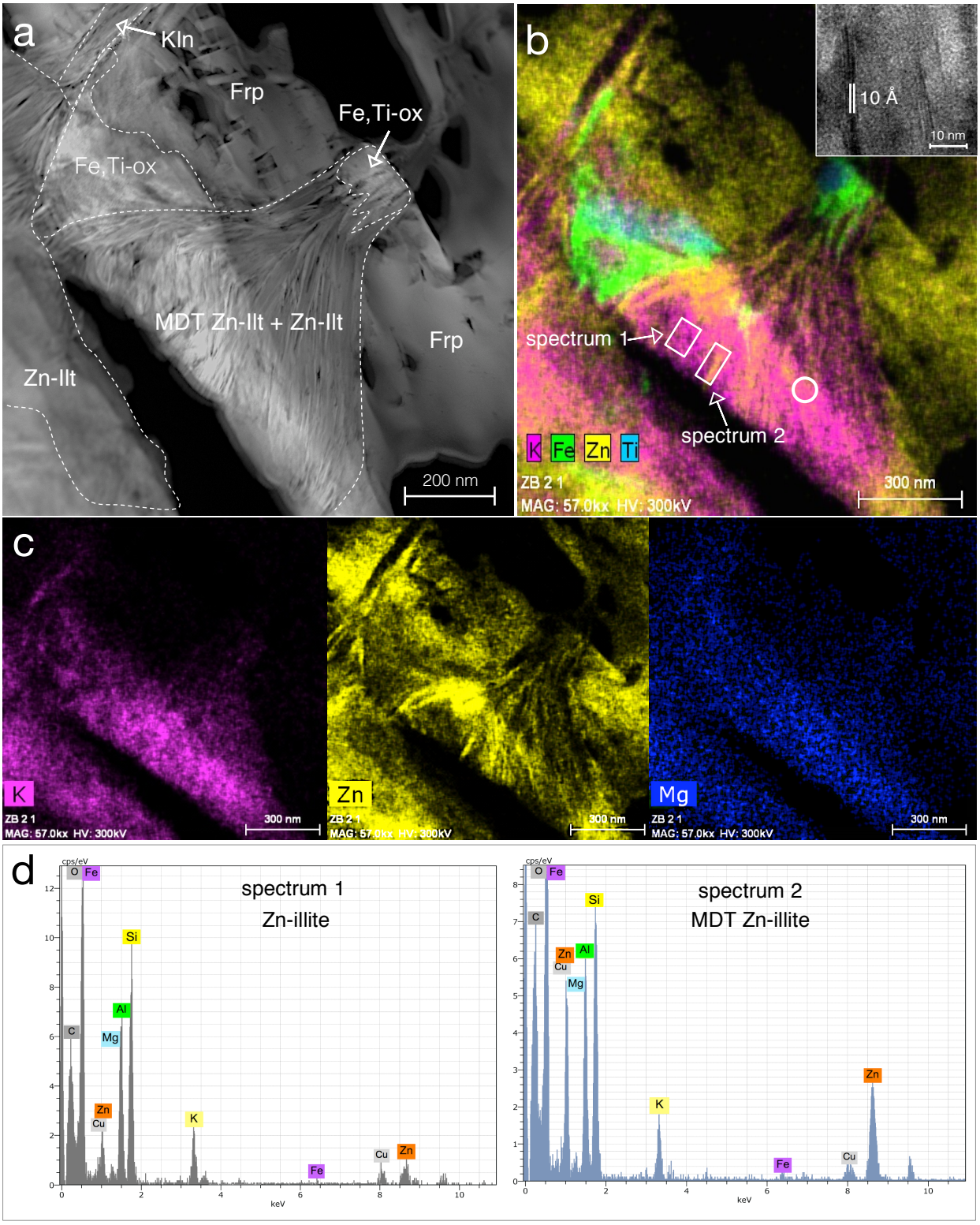
a
Kln
Frp
Fe,Ti-ox
Fe,Ti-ox
MDT Zn-Ilt + Zn-Ilt
Frp
Zn-Ilt
200 nm
b
10 Å
10 nm
spectrum 1
spectrum 2
K Fe Zn Ti
ZB 2 1
MAG: 57.0kx HV: 300kV
300 nm
c
K
ZB 2 1
MAG: 57.0kx HV: 300kV
300 nm
Zn
ZB 2 1
MAG: 57.0kx HV: 300kV
300 nm
Mg
ZB 2 1
MAG: 57.0kx HV: 300kV
300 nm
d
cps/eV
O Fe
Si
Al
C
Mg
Zn
Cu
K
Fe
Cu Zn
keV
spectrum 1
Zn-illite
cps/eV
O Fe
Si
C
Zn
Al
Cu
Mg
K
Fe
Cu
Zn
keV
spectrum 2
MDT Zn-illite

FIGURE 5

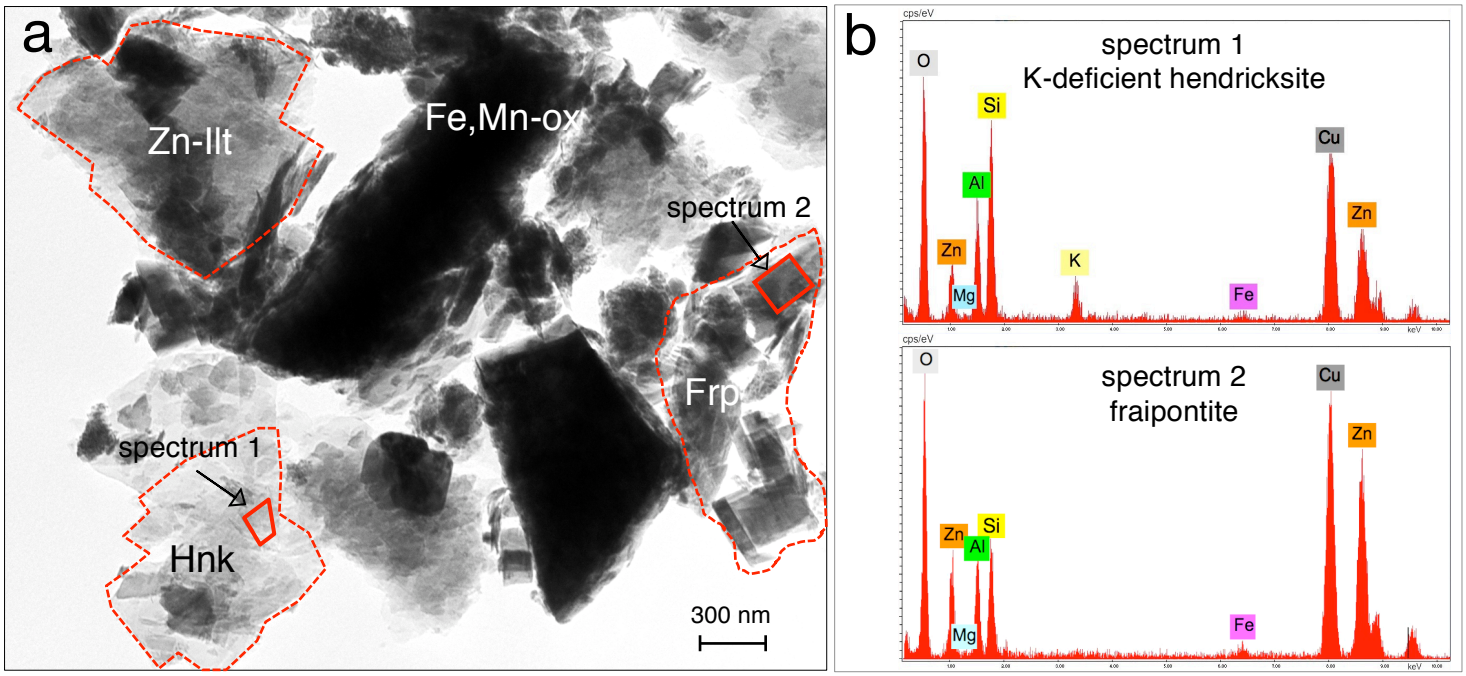
a
Zn-Ilt
Fe,Mn-ox
spectrum 2
Frp
spectrum 1
Hnk
300 nm
b
cps/eV
spectrum 1
K-deficient hendricksite
O
Si
Al
Cu
Zn
Zn
K
Mg
Fe
cps/eV
spectrum 2
fraipontite
O
Cu
Zn
Zn
Si
Al
Mg
Fe

FIGURE 6

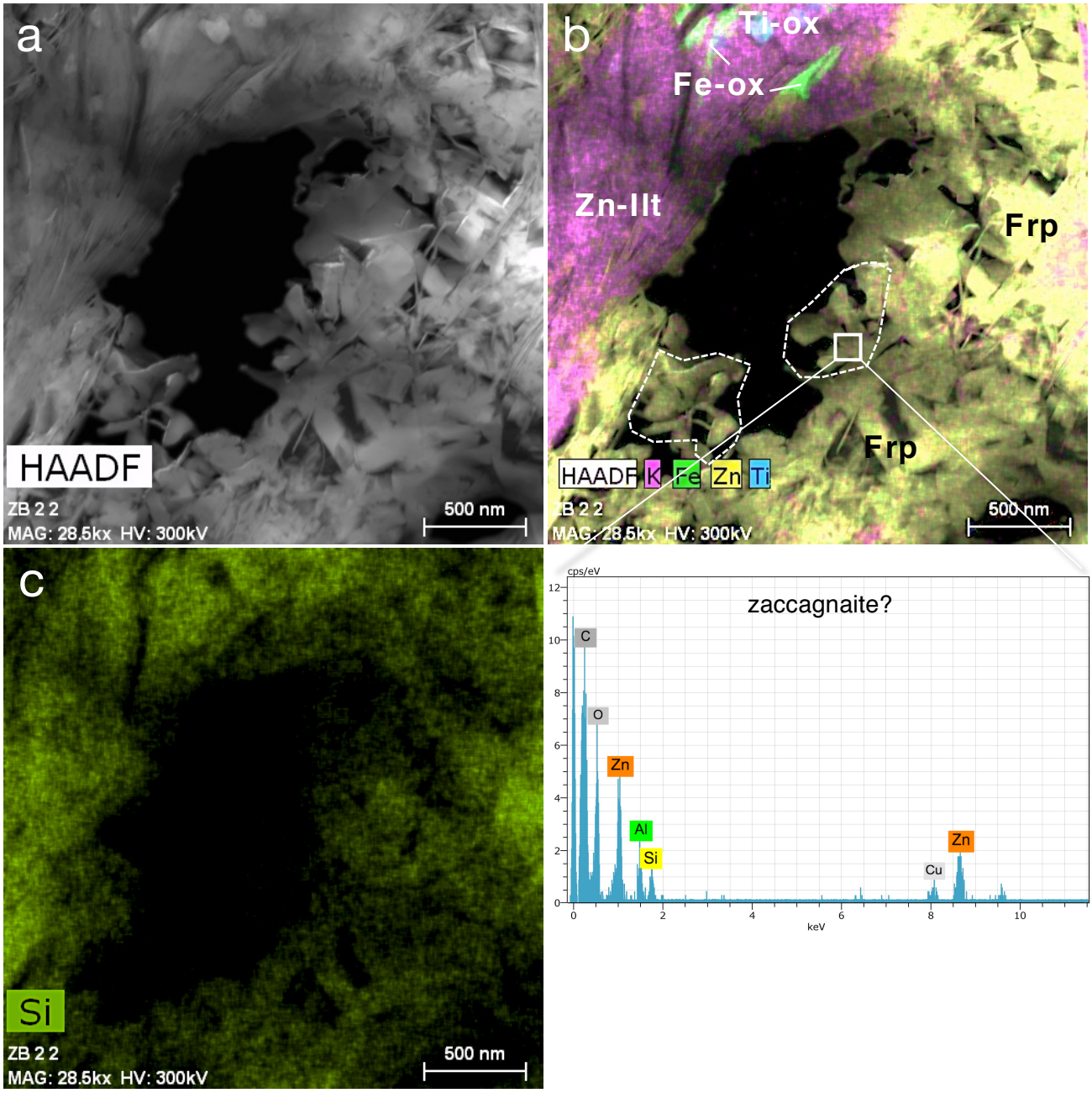
a
HAADF
ZB 2 2
MAG: 28.5kx HV: 300kV
500 nm
b
Ti-ox
Fe-ox
Zn-Ilt
Frp
Frp
HAADF K Fe Zn Ti
ZB 2 2
MAG: 28.5kx HV: 300kV
500 nm
c
Si
ZB 2 2
MAG: 28.5kx HV: 300kV
500 nm
cps/eV
zaccagnaite?
C
O
Zn
Al
Si
Cu
Zn
keV

FIGURE 7

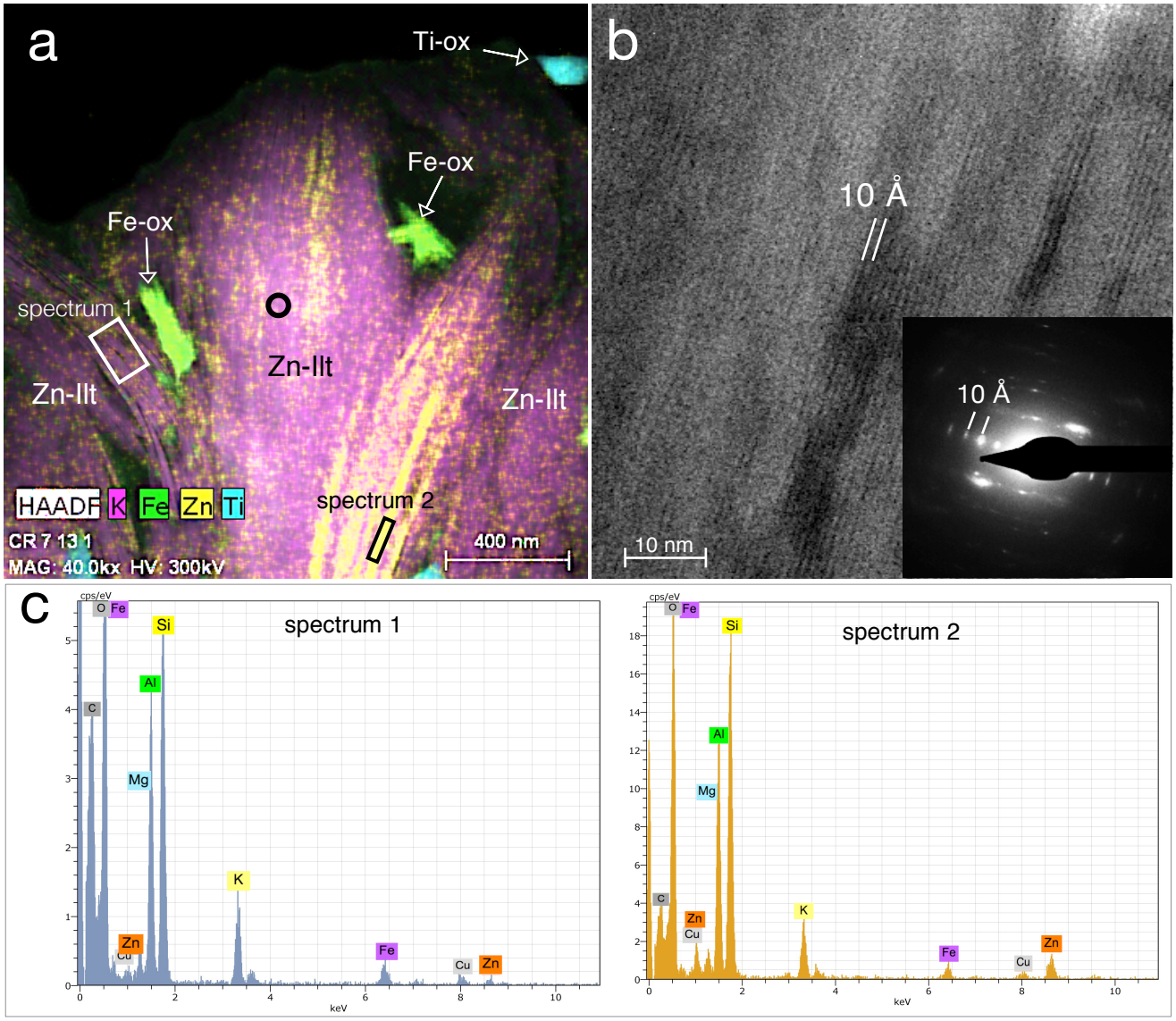
a
Ti-ox
Fe-ox
Fe-ox
spectrum 1
Zn-Ilt
Zn-Ilt
Zn-Ilt
HAADF K Fe Zn Ti
CR 7 13 1
MAG: 40.0kx HV: 300kV
spectrum 2
400 nm
b
10 Å
10 nm
10 Å
c
spectrum 1
spectrum 2
cps/eV
keV
O Fe
Si
Al
C
Mg
K
Zn
Cu
Fe
Cu
Zn

FIGURE 8

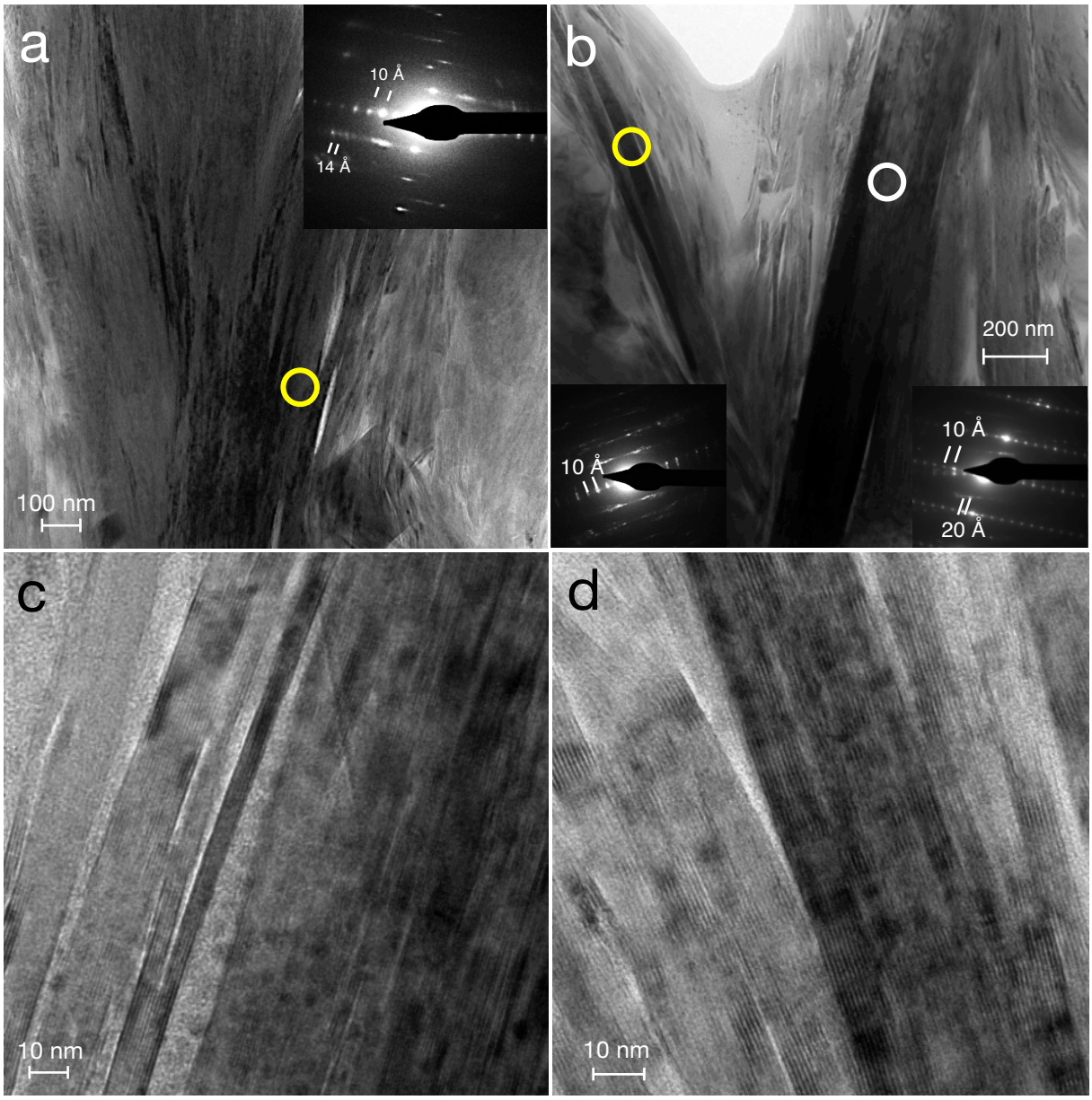

FIGURE 9

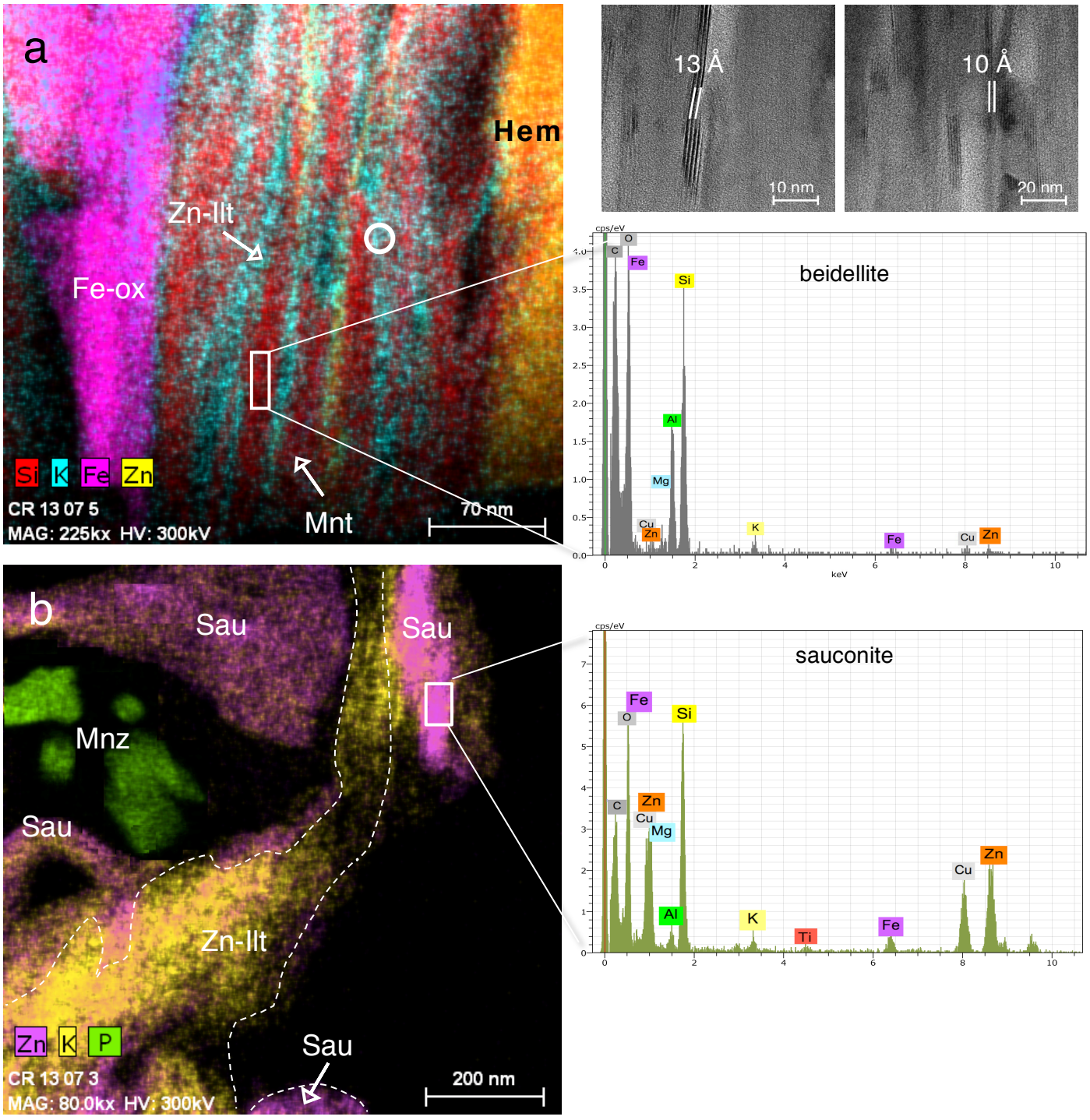
a
Hem
Zn-Ilt
O
Fe-ox
Si K Fe Zn
CR 13 07 5
MAG: 225kx HV: 300kV
Mnt
70 nm
13 Å
10 nm
10 Å
20 nm
cps/eV
beidellite
keV
b
Sau
Sau
Mnz
Sau
Zn-Ilt
Zn K P
CR 13 07 3
MAG: 80.0kx HV: 300kV
Sau
200 nm
sauconite

FIGURE 10

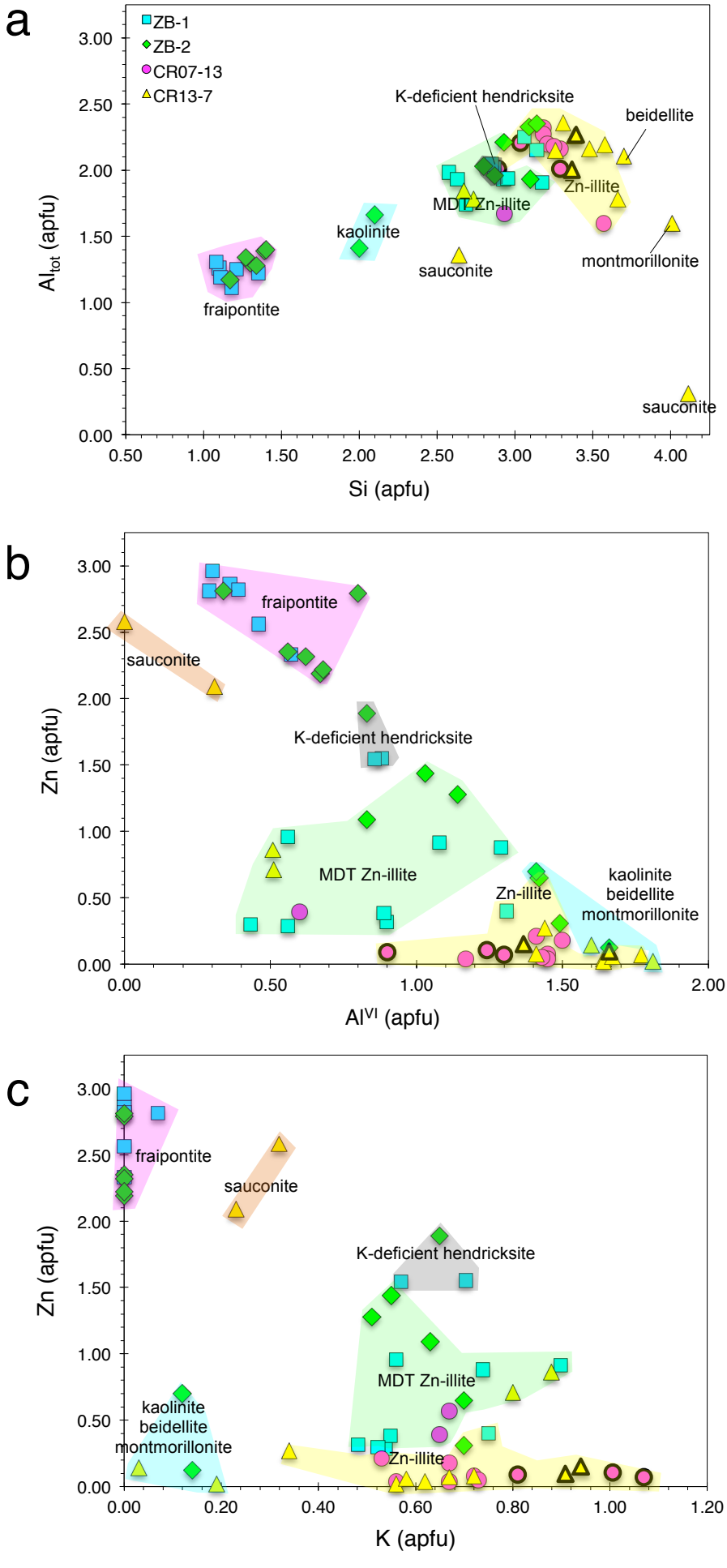
a
ZB-1
ZB-2
CR07-13
CR13-7
K-deficient hendricksite
beidellite
Zn-illite
MDT Zn-illite
kaolinite
sauconite
montmorillonite
fraipontite
sauconite
Al$_{tot}$ (apfu)
Si (apfu)
b
fraipontite
sauconite
K-deficient hendricksite
MDT Zn-illite
Zn-illite
kaolinite
beidellite
montmorillonite
Zn (apfu)
Al^{VI} (apfu)
c
fraipontite
sauconite
K-deficient hendricksite
MDT Zn-illite
kaolinite
beidellite
montmorillonite
Zn-illite
Zn (apfu)
K (apfu)

FIGURE 11

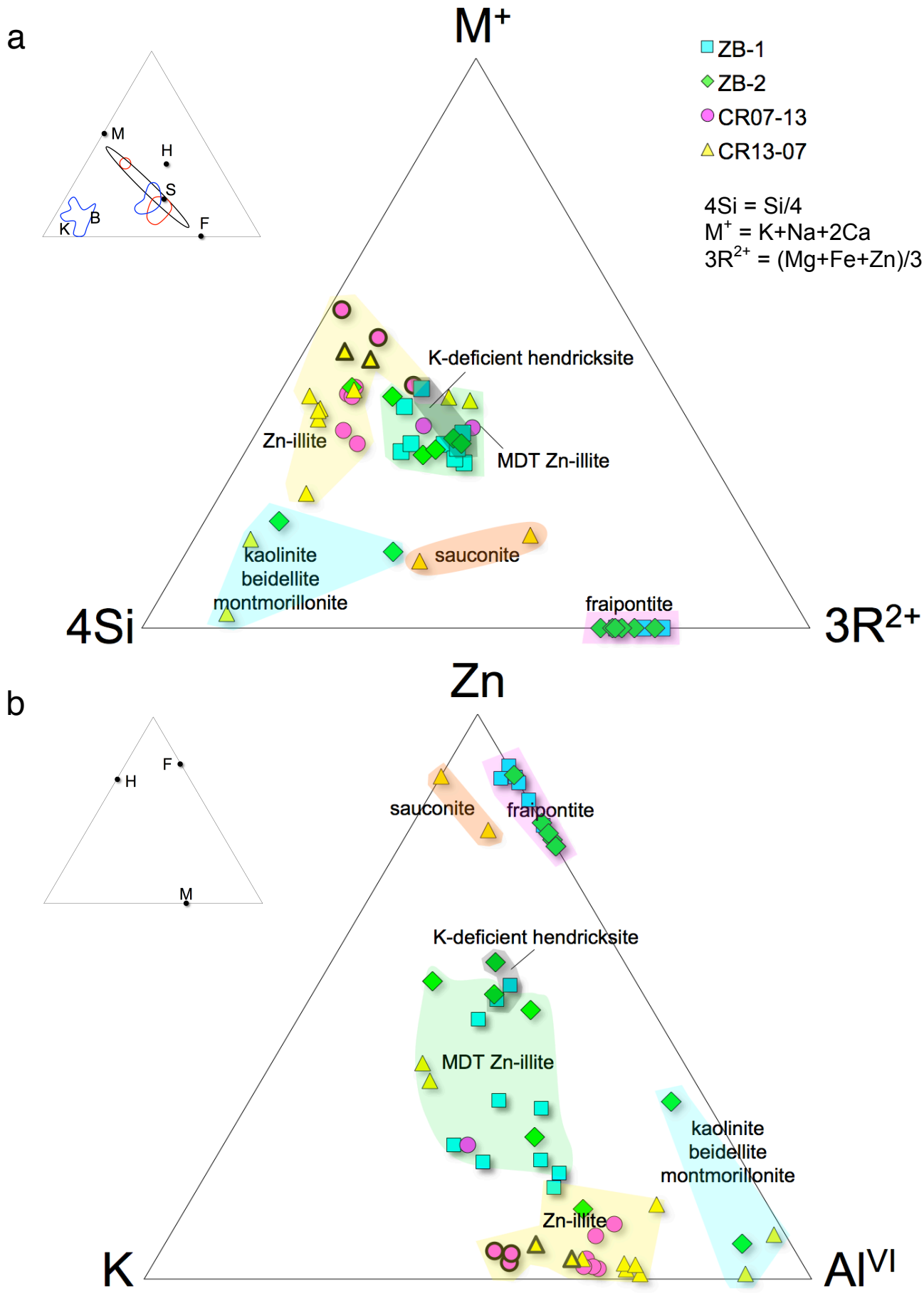
a
M+
ZB-1
ZB-2
CR07-13
CR13-07
4Si = Si/4
M+ = K+Na+2Ca
3R2+ = (Mg+Fe+Zn)/3
M
H
S
K
B
F
K-deficient hendricksite
Zn-illite
MDT Zn-illite
kaolinite
beidellite
montmorillonite
sauconite
fraipontite
4Si
3R2+
b
Zn
F
H
M
sauconite
fraipontite
K-deficient hendricksite
MDT Zn-illite
kaolinite
beidellite
montmorillonite
Zn-illite
K
AlVI

FIGURE 12

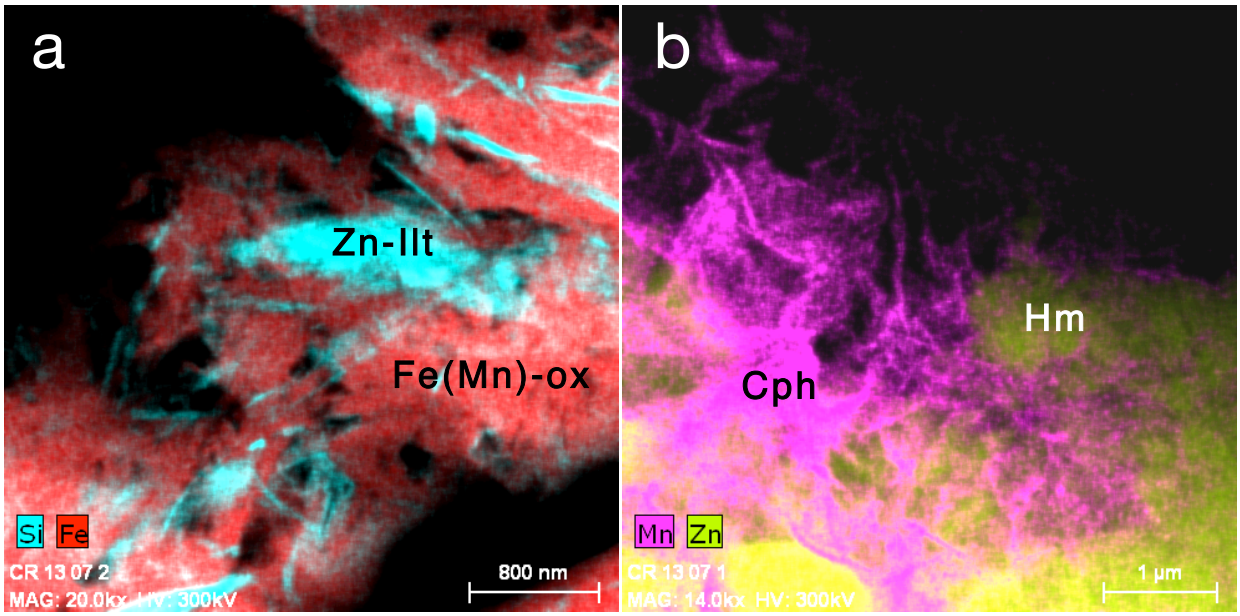
a
Zn-Ilt
Fe(Mn)-ox
Si Fe
CR 13 07 2
MAG: 20.0kx HV: 300kV
800 nm
b
Hm
Cph
Mn Zn
CR 13 07 1
MAG: 14.0kx HV: 300kV
1 µm

FIGURE 13